Draft version October 31, 2025
Typeset using LaTeX **twocolumn** style in AASTeX63

The $N_{\rm H}$ Distribution of Hard X-ray Selected AGN in the NEP Field

Samantha Creech,[1] Francesca Civano,[2] Daniel R. Wik,[1] Ross Silver,[2] Xiurui Zhao,[3,4] Rafael Ortiz III,[5] Tonima Ananna,[6] Norman A. Grogin,[7] Rolf Jansen,[5] Anton M. Koekemoer,[7] Christopher N.A. Willmer,[8] and Rogier A. Windhorst[5]

[1]*Department of Physics & Astronomy, The University of Utah, 115 South 1400 East, Salt Lake City, UT 84112, USA*
[2]*NASA Goddard Space Flight Center*
[3]*Department of Astronomy, University of Illinois at Urbana-Champaign, Urbana, IL 61801, USA*
[4]*Cahill Center for Astrophysics, California Institute of Technology, 1216 East California Boulevard, Pasadena, CA 91125, USA*
[5]*School of Earth and Space Exploration, Arizona State University, Tempe, AZ 85287-1404, USA*
[6]*Department of Physics and Astronomy, Wayne State University, Detroit, MI 48202, USA*
[7]*Space Telescope Science Institute, 3700 San Martin Drive, Baltimore, MD 21218, USA*
[8]*Steward Observatory, University of Arizona, 933 North Cherry Avenue, Tucson, AZ 85721, USA*

ABSTRACT

X-ray surveys are one of the most unbiased methods for detecting Compton Thick (CT; $N_{\rm H} \geq 10^{24}$ cm^{-2}) AGN, which are thought to comprise up to 60% of AGN within $z \lesssim 1.0$. These CT AGN are often difficult to detect with current instruments, but the X-ray data within the JWST-North Ecliptic Pole (NEP) Time Domain Field (TDF) present a unique opportunity to study faint and obscured AGN. The NEP contains the deepest NuSTAR survey to date, and Zhao et al. (2024) detected 60 hard X-ray sources from the combined exposure of NuSTAR's Cycle 5 and 6 observations. In this work, we utilize the NuSTAR Cycle 5+6+8+9 data and simultaneous XMM-Newton observations in order to perform the first spectroscopic analysis of the 60-source catalog. We present this analysis and measure the $N_{\rm H}$ distribution of the sample. We measure an observed CT fraction of $0.13^{+0.15}_{-0.04}$ down to an observed $8-24$ keV flux of 6.0×10^{-14} erg/s/cm^2, and we correct our analysis for absorption bias to estimate an underlying CT fraction of $0.32^{+0.23}_{-0.08}$. The derived obscuration distribution and CT fraction are consistent with population synthesis models and previous surveys.

Keywords: galaxy evolution: general; X-ray astronomy: general; galaxy clusters; general

1. INTRODUCTION

At the center of nearly every massive galaxy, we observe supermassive black holes (SMBHs) that are thought to co-evolve with their host galaxies (e.g. Ferrarese & Merritt 2000; Gebhardt et al. 2000; Kormendy & Ho 2013). Accretion is the primary channel of black hole growth (e.g. Soltan 1982), and during phases of high accretion, the SMBH is classified as an active galactic nucleus (AGN). These accretion processes power AGN emission across the entire electromagnetic spectrum. In the X-ray band, emission is produced by the corona: a reservoir of relativistic electrons located within a light hour of the SMBH (e.g Martocchia & Matt 1996; Fabian et al. 2009). X-rays are produced when optical and UV emission from the accretion disk is Comptonized by the corona (e.g. Haardt & Maraschi 1991), resulting in a powerlaw spectrum. However, for many AGN, the intrinsic powerlaw emission is reprocessed via the photoelectric effect and Compton scattering by an obscuring region, which is known as the obscuring torus in typical models of AGN unification (e.g. Turner et al. 1997; Risaliti et al. 1999; Brightman & Nandra 2011). The features of the observed X-ray spectrum are sensitive to the geometrical properties of the obscuring torus, particularly the line-of-sight column density ($N_{\rm H(los)}$; $N_{\rm H}$ for brevity). When $N_{\rm H} < 10^{22}$ cm^{-2}, the AGN is dubbed unabsorbed. Between 10^{22} cm$^{-2} \leq N_{\rm H} < 10^{24}$ cm^{-2}, the AGN is classified as Compton Thin (C-Thin) or obscured. In the most extreme case, when $N_{\rm H} \geq 1/\sigma_T \sim 10^{24}$ cm^{-2}, where σ_T is the Thomson cross-section for electron scattering, the AGN is classified as Compton Thick (CT). At these high column densities, the soft-band emission ($\lesssim$ 5keV) is heavily suppressed, and the observed soft X-ray emission is 30-50 times fainter than the intrinsic X-ray luminosity (L_X; see Figure 4 from Ananna et al. 2022), making it difficult to identify the full CT population. While hard X-rays ($\geq$ 10 keV) are attenuated in the most extreme cases, they are less affected than the soft X-ray band (e.g. Ueda et al. 2014,

Figure 7), so deep exposures in this band are an excellent tool to study the properties of the full AGN population, including CT AGN.

Studying AGN above 10 keV also helps us understand the Cosmic X-ray Background (CXB), i.e. the diffuse X-ray emission covering the entire sky in the ∼1-300 keV band. The vast majority of the CXB is unresolved emission of faint AGN. As a result, the CXB probes the full AGN population and has provided constraints for models of SMBH growth (e.g. Comastri et al. 1995; Gilli et al. 2007; Ueda et al. 2014; Ananna et al. 2019; Gerolymatou et al. 2025). In particular, the peak of the CXB spectrum around $20-30$keV (e.g, Rossland et al. 2023) requires that a sizable fraction of AGN must be CT (Comastri et al. 1995; Gilli et al. 2007; Ueda et al. 2014; Ananna et al. 2019; Gerolymatou et al. 2025). The CT fraction (f_{CT}, which we define as the fraction of all AGN with $N_{\rm H} > 10^{24}$ cm^{-2}; $N_{\rm CT}/N_{\rm total}$) is an important component of SMBH population synthesis models, but measuring f_{CT} from the CXB yields large uncertainties (Gilli et al. 2007; Treister et al. 2009; Ueda et al. 2014). In order to accurately constrain f_{CT}, it is necessary to resolve the AGN population that comprises the CXB. AGN X-ray surveys are one of the best methods to accomplish this.

Previous surveys in the X-ray band have yielded constraints on f_{CT}. Lansbury et al. (2017) finds $f_{CT} = 0.3$ using the 40-month Serendipitous survey ($z \lesssim 0.1$). In the NuSTAR-COSMOS survey ($z \sim 0.5$), Civano et al. (2015) finds $f_{CT} = 0.13 \pm 0.03$ or $f_{CT} = 0.20 \pm 0.03$ based on a single CT detection. Chandra observations of radio-selected galaxies at $0.5 < z < 1$ yielded $f_{CT} \sim 0.20$ (Kuraszkiewicz et al. 2021), and a similar result was found for radio-selected galaxies at higher redshifts ($1 < z < 2$; Wilkes et al. 2013). From the combined source catalogs of the NuSTAR extragalactic surveys, Zappacosta et al. (2018) finds the CT fraction to be between $f_{CT} = 0.02-0.56$ ($z \sim 0.5$). From the Ultra Deep Field survey (UDF), Masini et al. (2018) finds $f_{CT} = 0.13 \pm 0.02$ ($z \sim 1$). Torres-Albà et al. (2021) estimates that $\sim 8\%$ of sources detected by the Swift-BAT survey ($z \leq 0.05$) are CT, while Akylas et al. (2024) estimates a local fraction $f_{CT} = 25-30\%$ by folding the BAT survey with mid-IR-selected AGN. Carroll et al. (2023) fuses joint Mid-IR and X-ray properties to find $f_{CT} = 0.555^{+0.040}_{-0.030}$. Most recently, Boorman et al. (2025) finds $f_{CT} = 0.35 \pm 0.09$ using local, NuSTAR-detected AGN selected by IR properties.

Several of these surveys utilize NuSTAR, which is the first X-ray telescope able to focus AGN emission at energies > 10 keV. The NuSTAR extragalactic surveys have followed a "wedding cake" strategy by combining relatively shallow observations of wide fields with deep, narrow surveys. The wide layers of the wedding cake include the COSMOS Legacy survey (1.7 deg^{-2}; Civano et al. 2015) and the Serendipitous survey (13 deg^{-2}; Alexander et al. 2013; Lansbury et al. 2017). The deep, narrow layers include the Extended Chandra Deep Field-South (~ 0.33 deg^{-2}; Mullaney et al. 2015) and the UDF (0.6 deg^{-2}; Masini et al. 2018).

The JWST-North Ecliptic Pole Time Domain Field (NEP; 0.3 deg^{-2}) is a recent addition to the wedding cake. With 3.5 Ms of exposure time across five contiguous years, the NEP field hosts the deepest NuSTAR survey to date. The first results of the NuSTAR Cycle 5 data are presented by Zhao et al. (2021), the Cycle 5+6 analysis is presented by Zhao et al. (2024) (Z24 hereafter), and Cycle 8+9 is discussed in Silver et al. (2025). Z24 identified 60 sources from the combined Cycle 5+6 NuSTAR observations. Hardness ratios—which give the relative difference between the 3-8 and 8-24 keV bands—yield predicted $N_{\rm H}$ values for the sources, and Z24 uses these hardness ratios to estimate $f_{CT} = 0.18^{+0.20}_{-0.08}$. In this work, we follow up on the Z24 catalog by presenting the first NuSTAR+XMM-Newton spectral analysis of these 60 sources, and we calculate the obscuration distribution and f_{CT} of the sample.

In Section 2, we describe the sample, observations, and data reduction. In Section 3, we define the models used to analyze our X-ray spectra and explain our fitting methods. We calculate the $N_{\rm H}$ distribution in Section 4 and discuss the implications in Section 5. Our findings are summarized in Section 6. This study assumes a ΛCDM cosmology with $H_0 = 70$ km s^{-1} Mpc^{-1}, $\Omega_M = 0.27$, and $\Omega_\Lambda = 0.73$ (Planck Collaboration et al. 2020).

2. SAMPLE AND DATA REDUCTION

The observation IDs used in this analysis are listed in Table 1, and the sources from the Z24 catalog are summarized in Table 2. The following procedure uses all available NuSTAR data (Cycles 5+6+8+9) and XMM-Newton observations in order to extract spectra for these 60 sources.

2.1. *NuSTAR*

The observations of the NuSTAR-NEP survey were taken in fifteen epochs, with three or four observations per epoch (Table 1). These epochs took place during NuSTAR Cycle 5 (PI: Civano, ID: 5192), Cycle 6 (PI: Civano, ID: 6218), Cycle 8 (PI: Civano, ID: 8180), and Cycle 9 (PI: Civano, ID: 9267). Data reduction was performed by Zhao et al. (2021) (Cycle 5), Z24 (Cycle 6), and Silver et al. (2025) (Cycles 8 and 9). We discuss relevant details here.

Table 1. NuSTAR and XMM-Newton Observations of the NEP

Cycle	Epoch	Date	NuSTAR IDs	XMM-Newton ID
5	1	09/2019	60511001002, 60511002002, 60511003002	-
	2	01/2020	60511004002, 60511005002, 60511006002	-
	3	03/2020	60511007002, 60511008001, 60511009001	-
6	4	10/2020	60666001002, 60666002002, 60666003002	0870860101
	5	01/2021	60666004002, 60666005002, 60666006002	0870860201
	6	10/2021	60666007002, 60666008002, 60666009002	-
	7	01/2022	60666010002, 60666011002, 60666012002	0870860401
8	8	08/2022	60666013002, 60666014002, 60666015002	0870860501
	9	11/2022	60810001002, 60810002002, 60810003002	0913590101
	10	02/2023	60810004002, 60810005002, 60810006002	0913590501
	11	05/2023	60810007002, 60810008002, 60810009002, 60810009004	0913590601
9	12	08/2023	60910001002, 60910002002, 60910003002, 60910001004	0931420701
	13	11/2023	60910004002, 60910005002, 60910006002	0931420101
	14	05/2024	60910007002, 60910008002, 60910009002	0931420101
	15	02/2024	60910010002, 60910011002, 60910012002	0931420501

The NuSTAR data were processed using HEASOFT (v.27.2, v.6.29c, and v.6.33.1) and CALDB (v.202005266, v.20211115, and v.20230816). Data from all observations were calibrated, cleaned, and screened using NUPIPELINE. Time intervals with high background were removed by screening for periods in which the 3.5-9.5 keV count rate was ≥ 2 times higher than the average value within the entire observation.

Vignetted exposure maps were produced using the NUEXPOMAP tool from NuSTARDAS. Background maps were created using NUSKYBGD[1] (Wik et al. 2014). We refer to Zhao et al. (2021), Z24, and Silver et al. (2025) for further details.

For spectral extraction, region sizes were chosen to maximize individual source signal-to-noise (see Appendix A for details), and NUPRODUCTS was used to extract higher level data products from the exposure-corrected NuSTAR data. Background spectra were extracted using the NUBGDSPEC routine from NUSKYBGD (Wik et al. 2014). In instances where background-subtracted spectra had net zero or negative source photons—implying that the spectrum is background-dominated—that observation was excluded from the analysis of the source.

Finally, the spectra from all observations were added using the ADDSPEC python routine[2]. FPMA and FPMB were kept separate. In this paper, we assume that all the sources have zero variability and combine spectra from all epochs to improve count statistics. Z24 discusses variability analysis.

[1] https://github.com/NuSTAR/nuskybgd

[2] https://github.com/JohannesBuchner/addspec.py

2.2. *XMM-Newton*

XMM-Newton observations were timed such that they aligned with the NuSTAR epochs in Cycles 6, 8, and 9 (see Table 1). One XMM-Newton observation (Obs. ID 0870860301; NuSTAR epoch 6) was background dominated and not included in any analysis. Otherwise, each epoch in NuSTAR cycles 6, 8, and 9 have a corresponding XMM-Newton observation, which were reduced by Z24 (Cycle 6) and Silver et al. (2025) (Cycles 8 and 9) using the XMM-Newton Science Analysis System (SAS; version 20.0.0) and following the procedures outlined by Brunner et al. (2008), Cappelluti et al. (2009), and LaMassa et al. (2009). The tasks EMPROC and EPPROC were used to create observational data files of the three instruments (MOS1, MOS2, and PN), from which high background time intervals and fluorescent emission line energy bands were excluded. From the clean event files, images were generated for all three instruments in the 0.5-2 keV and 2-10 keV energy bands. For both of these energy bands, exposure maps were generated using SAS EEXPMAP task. After masking potential X-ray sources identified by EBOXDETECT, background maps were generated for all three instruments using ESPLINEMAP, with FITMETHOD = model. This models the XMM-Newton background with a detector component and a CXB component.

Out of the 60 NuSTAR-identified sources in the Z24 catalog, 36 have lower-energy XMM-Newton counterparts. XMM-Newton spectra were extracted using 15″

source regions centered around the coordinates of the XMM-Newton sources, and local backgrounds were extracted from 75-100″ annuli. XMM-Newton has a smaller PSF (FWHM $5-6''$) and does not require the SNR-maximized region method used for NuSTAR. The EVSELECT routine was used to extract source and background spectra from MOS1, MOS2, and PN. The scaling factor for normalizing the background spectrum was calculated using the BACKSCALE routine. The RMFGEN and ARFGEN tasks generated RMFs and ARFs, respectively. In order to account for the cross calibration between NuSTAR and XMM-Newton instruments, we applied the flags APPLYABSFLUXCORR=YES (which corrects the effective area of PN spectra in order to better match NuSTAR) and APPLYXCALADJUSTMENT=YES (which improves consistency between MOS and PN spectra by applying an energy-dependent correction function) to the ARFGEN routine.

Table 2. AGN Properties

Nu ID[a]	XMM ID[ab]	Nu net cts	XMM net cts	RA [deg]	DEC [deg]	$_z$[c]	F_{obs}^{2-10} [erg/s/cm^2]	L_{obs}^{2-10} [erg/s]	F_{obs}^{3-24} [erg/s/cm^2]	L_{obs}^{3-24} [erg/s]	F_{obs}^{8-24} [erg/s/cm^2]	L_{obs}^{8-24} [erg/s]	Class[d]
1	-	37.2	-	260.530704	66.059882	-	-	-	1.69e-13	-	2.08e-13	-	-
2	4	476.7	1148.9	261.004963	66.012388	0.892^{S}	6.01e-14	2.37E+44	1.07e-13	4.21E+44	1.3e-13	5.12E+44	Q (Z24)
3	60	183.4	66.1	260.615623	65.980155	0.0^{S}	1.23e-14	-	2.8e-14	-	4.27e-14	-	S (Z24)
4	-	424.4	-	260.74987	65.968707	-	-	-	2.35e-14	-	3.24e-14	-	-
5	-	149.9	-	260.434776	65.961318	-	-	-	2.9e-14	-	3.85e-14	-	-
6	37	575.0	200.3	260.522038	65.954027	0.62^{P}	2.66e-14	4.30E+43	7.39e-14	1.19E+44	4.98e-14	8.04E+43	Q (O26)
7	34	304.9	94.6	260.468713	65.93478	0.27^{S}	9.43e-15	2.14E+42	2.28e-14	5.16E+42	3.5e-14	7.93E+42	G (Z24)
8	97	160.3	30.8	260.622873	65.923493	0.81^{P}	8.72e-15	2.71E+43	1.29e-14	4.01E+43	2.1e-14	6.52E+43	Q (O26)
9	-	114.6	-	261.188068	65.881698	-	-	-	7.26e-14	-	1.1e-13	-	-
10	240	188.3	48.1	260.544655	65.887843	-	4.48e-15	-	1.29e-14	-	2.02e-14	-	-
11	32/138	231.0	246.7	260.73184	65.89017	0.601^{S}	9.33e-15	1.40E+43	1.26e-14	1.89E+43	1.76e-14	2.63E+43	Q (Z24)
12	26	322.9	106.1	260.466229	65.879465	5.35^{P}	7.98e-15	2.44E+45	2.26e-14	6.90E+45	3.2e-14	9.76E+45	Q (O26)
13	63/76	368.5	188.4	260.783715	65.872453	-	4.74e-15	-	1.38e-14	-	1.93e-14	-	-
14	-	278.1	-	260.359797	65.853886	-	-	-	2.89e-14	-	4.34e-14	-	-
15	56	140.4	60.4	260.539214	65.790189	2.251^{S}	8.73e-15	3.37E+44	1.57e-14	6.05E+44	1.98e-14	7.64E+44	Q (Z24)
16	-	216.5	-	261.103491	65.770554	-	-	-	5.21e-14	-	6.81e-14	-	-
17	-	254.0	-	260.978502	65.723582	-	-	-	3.53e-14	-	3.29e-14	-	-
18	-	146.2	-	260.403922	65.720876	-	-	-	4.58e-14	-	7.35e-14	-	-
19	49	855.5	207.2	260.689412	65.740591	1.32^{P}	1.85e-14	1.92E+44	3.7e-14	3.84E+44	3.45e-14	3.58E+44	Q (O26)
20	11	158.5	220.3	260.867239	65.982407	1.425^{S}	1.58e-14	1.98E+44	7.15e-14	8.97E+44	7.33e-14	9.20E+44	Q (Z24)
21	12	408.9	607.3	260.823684	65.944847	0.495^{S}	2.47e-14	2.32E+43	3.96e-14	3.71E+43	2.84e-14	2.66E+43	G (Z24)
22	47	382.2	123.4	260.656285	65.931053	1.23^{P}	1.44e-14	1.26E+44	4.89e-14	4.26E+44	2.8e-14	2.44E+44	Q (O26)
23	112/165	214.3	117.2	260.495899	65.907535	-	6.11e-15	-	2.1e-14	-	7.65e-15	-	-
24	3	347.7	1451.7	260.42374	65.921001	0.523^{S}	6.11e-14	6.54E+43	8.88e-14	9.50E+43	4.4e-14	4.71E+43	Q (Z24)
25	-	196.0	-	261.194464	65.859152	-	-	-	1.03e-13	-	8.76e-14	-	-
26	36	243.6	165.9	261.025736	65.842349	1.8^{P}	2.1e-14	4.69E+44	2.15e-14	4.80E+44	1.8e-14	4.02E+44	Q (O26)
27	-	414.6	-	260.523638	65.834538	-	-	-	1.37e-14	-	1.17e-14	-	-
28	7	557.8	495.3	260.965651	65.836937	0.673^{S}	2.01e-14	3.96E+43	3.15e-14	6.21E+43	1.48e-14	2.92E+43	Q (Z24)
29	1	8447.9	7746.7	260.808941	65.796673	1.441^{S}	1.51e-13	1.95E+45	2.79e-13	3.60E+45	1.65e-13	2.13E+45	Q (Z24)
30	73	299.4	77.7	260.44349	65.839801	1.68^{P}	1.5e-14	2.82E+44	1.62e-14	3.05E+44	1.5e-14	2.82E+44	Q (O26)
31	51/64	411.1	85.0	261.078906	65.815655	0.376^{S}	2.13e-14	1.04E+43	4.89e-14	2.39E+43	2.39e-14	1.17E+43	G (Z24)
32	69	334.1	122.2	260.695612	65.808196	1.83^{P}	5.69e-15	1.32E+44	1.47e-14	3.42E+44	7.13e-15	1.66E+44	Q (O26)
33	-	126.1	-	261.11552	65.810138	-	-	-	6.96e-14	-	5.17e-14	-	-
34	169	181.0	128.5	260.885542	65.781661	0.403^{S}	6.49e-15	3.73E+42	1.12e-14	6.44E+42	9.14e-15	5.25E+42	G (Z24)
35	-	146.2	-	260.53465	65.756721	-	-	-	2.68e-14	-	1.54e-14	-	-
36	66	457.4	68.2	260.58976	65.734981	1.019^{S}	1.18e-14	6.46E+43	1.79e-14	9.80E+43	2.23e-14	1.22E+44	Q (Z24)
37	205	299.5	74.1	261.035039	65.734455	0.85^{P}	2.17e-14	7.59E+43	3.49e-14	1.22E+44	3.37e-14	1.18E+44	Q (O26)
38	-	415.5	-	261.006258	65.635478	-	-	-	2.56e-13	-	2.14e-13	-	-
39	99	124.3	19.9	260.70263	66.014412	4.35^{P}	9.99e-15	1.87E+45	7.78e-14	1.46E+46	1.07e-13	2.01E+46	Q (O26)
40	-	161.9	-	260.99109	65.922953	-	-	-	3.86e-14	-	3.72e-14	-	-
41	10/203	346.0	470.6	260.751816	65.908622	-	1.29e-14	-	2.3e-14	-	1.93e-14	-	-
42	-	122.6	-	261.054304	65.870312	-	-	-	3.03e-14	-	3.11e-14	-	-
43	5	684.6	1569.3	260.638622	65.84636	1.337^{S}	2.22e-14	2.38E+44	2.35e-14	2.52E+44	1.48e-14	1.59E+44	Q (Z24)
44	-	312.0	-	260.718727	65.845092	-	-	-	1.5e-14	-	1.45e-14	-	-
45	141	482.6	94.0	260.990613	65.824629	1.35^{P}	7.99e-15	8.77E+43	4.52e-14	4.96E+44	3.05e-14	3.35E+44	Q (O26)
46	54/65	254.6	0.0	260.769055	65.77412	0.634^{S}	8.06e-15	1.37E+43	3.05e-14	5.20E+43	2.27e-14	3.87E+43	Q (Z24)
47	-	396.8	-	260.767207	65.821916	-	-	-	2.15e-14	-	1.42e-14	-	-
48	-	262.0	-	260.673401	65.659318	-	-	-	6.31e-14	-	1.01e-13	-	-
49	-	199.7	-	260.982765	65.932518	-	-	-	3.86e-14	-	5.12e-14	-	-
50	-	240.6	-	260.801946	65.929818	-	-	-	1.56e-14	-	2.03e-14	-	-

Table 2 *continued*

Table 2 *(continued)*

51	134/181	227.9	14.7	260.557293	65.948639	0.47[p]	8.27e-15	6.85E+42	3.46e-14	2.86E+43	4.92e-14	4.07E+43	N/A (Z24)
52	-	227.9	-	260.823766	65.895685	-	-	-	1.44e-14	-	2.42e-14	-	-
53	13	983.6	256.5	260.778758	65.856746	0.885[s]	2.73e-14	1.05E+44	6.85e-14	2.65E+44	4.76e-14	1.84E+44	Q (Z24)
54	14	547.4	326.5	260.893905	65.819897	0.779[s]	2.41e-14	6.80E+43	1.62e-14	4.57E+43	2.2e-14	6.21E+43	G (Z24)
55	2	1778.1	2622.3	260.429729	65.766017	0.781[s]	1.01e-13	2.87E+44	1.59e-13	4.52E+44	9.55e-14	2.71E+44	Q (Z24)
56	-	242.3	-	260.566157	65.764297	-	-	-	1.56e-14	-	3.25e-14	-	-
57	28	359.4	131.1	260.493365	65.736825	1.349[s]	1.12e-14	1.23E+44	3.28e-14	3.59E+44	3.11e-14	3.41E+44	Q (O26)
58	17	2586.7	577.1	260.671348	65.711891	0.179[s]	5.16e-14	4.63E+42	1.98e-13	1.78E+43	1.44e-13	1.29E+43	G (Z24)
59	-	178.8	-	260.807485	65.705176	-	-	-	3.55e-14	-	5.22e-14	-	-
60	42	255.8	0.0	260.726199	65.698978	0.44[p]	1.11e-14	7.85E+42	3.08e-14	2.18E+43	5.02e-14	3.55E+43	N/A (Z24)

Note—
[a] NuSTAR and XMM-Newton IDs from the Z24 catalog
[b] For sources with more than one XMM-Newton match, both are listed. The first match is used for the analysis.
[c] superscript denotes method for redshift measurment (p for photometric, s for spectroscopic)
[d] S for Star, Q for Quasar, G for Galaxy, N/A for unidentified. In parentheses, the work that presents the classification (Z24 or O26) is cited. Table 3 gives SED inferences for sources classified by O26.

2.3. *Multi-Wavelength Counterparts*

Of the 60 sources in the Z24 catalog, 33 have multi-wavelength matches, which allow redshifts and classification to be inferred. The redshift and luminosity distributions for these 33 sources are shown in Figure 1.

Z24 identified 21 multi-wavelength counterparts, which provide spectroscopic redshifts. These sources are identified as quasars (which have broad emission lines), composite galaxies (including Type II AGN and star forming galaxies with narrow emission lines), or stars. Z24 classifies objects by cross-correlating optical counterparts against SDSS template spectra[3].

In addition to the 21 counterparts identified by Z24, Ortiz et al. *in prep* (O26 hereafter) cross-matches eleven sources with recent catalogs. One source (AGN 57) is matched with the DESI DR1 catalog (DESI Collaboration et al. 2025) and has a corresponding spectroscopic redshift. Eleven sources have counterparts in the JWST and HST footprints (O26). Photometric redshifts and galaxy types are inferred using SED inferences from X-CIGALE (Boquien et al. 2019; Yang et al. 2020) using all available broadband photometry from space (JWST (Windhorst et al. 2023, Jansen et al *in prep*)); HST (O'Brien et al. 2024); WISE (Schlafly et al. 2019)) and the ground (HSC (Aihara et al. 2018), SDSS (Abdurro'uf et al. 2022), MMT (Willmer et al. 2023), JPAS (Hernán-Caballero et al. 2023)). The parameters of interest from SED fitting are the photometric redshift quality parameter Q_z (see equation 8 of Brammer et al. 2008) and f_{AGN} (fractional contribution of the AGN SED to the 0.1-30 μm bolometric luminosity), which we use to classify objects. Sources with $f_{AGN} > 0.2$ are generally inferred to be QSOs, but due to large uncertainties ($\sim$ 5-10%; Ciesla et al. 2015), we require $f_{AGN} > 0.3$ for QSO classification; otherwise, the source is classified as a composite galaxy. These relevant details are summarized in Table 3. Full details on the catalog creation and SED fitting are to be discussed in O26.

[3] https://classic.sdss.org/dr5/algorithms/spectemplates/

Table 3. O26 SED inferences

Nu ID	z	f_{AGN}[a]	Class[b]	Q_z[c]
6	0.62	0.233	G	0.07
8	0.81	0.414	Q	0.14
12	5.35	0.233	G	2.94
19	1.32	0.527	Q	0.8
22	1.23	0.498	Q	0.43
26	1.8	0.441	Q	1.17
30	1.68	0.569	Q	2.06
32	1.83	0.303	Q	1.97
37	0.85	0.382	Q	0.31
39	4.35	0.201	G	1.20
45	1.35	0.345	Q	0.07
57	1.35	0.384	Q	-[d]

[a] fraction of emission attributed to AGN
[b] Q for Quasar, G for Galaxy
[c] Redshift quality parameter (Brammer et al. 2008), with $Q_z < 1$ deemed reliable
[d] AGN 57 has a spectroscopic redshift from DESI Collaboration et al. (2025), so Q_z is not listed

3. SPECTRAL ANALYSIS

Together, NuSTAR and XMM-Newton spectra cover a $0.1 - 24.0$ keV energy range. Figure 2 shows the net spectral counts. Of the 36 sources with XMM-Newton counterparts, 27 have more NuSTAR counts than XMM-Newton counts; this is because most of the NuSTAR source regions are larger than the 15″ XMM-Newton regions (Appendix A). For spectral fitting, the count differences are corrected by the effective area encoded in the ARF files.

3.1. *Components of AGN X-ray Spectra*

In this work, X-ray spectra are described using three additive components: a transmitted powerlaw, a scat-

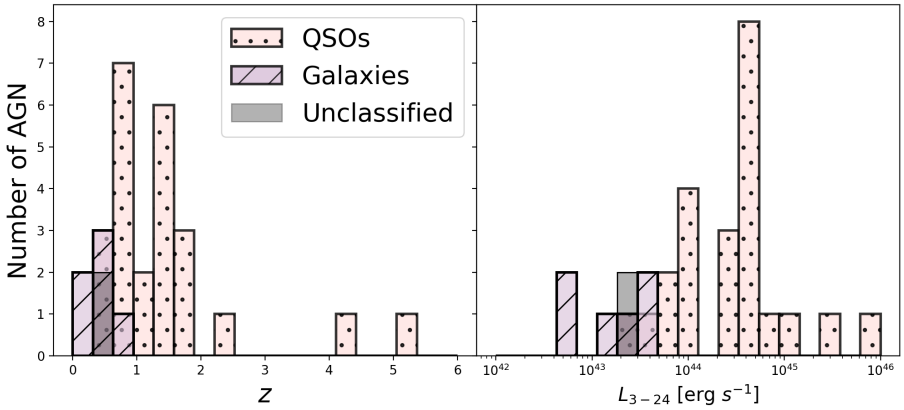

Figure 1. The redshifts (left) and observed 3-24 keV X-ray luminosities (right) for sources with detected multi-wavelength counterparts. Shown are quasars (dotted; pink), galaxies (hashed; purple), and unclassified (solid; gray) objects.

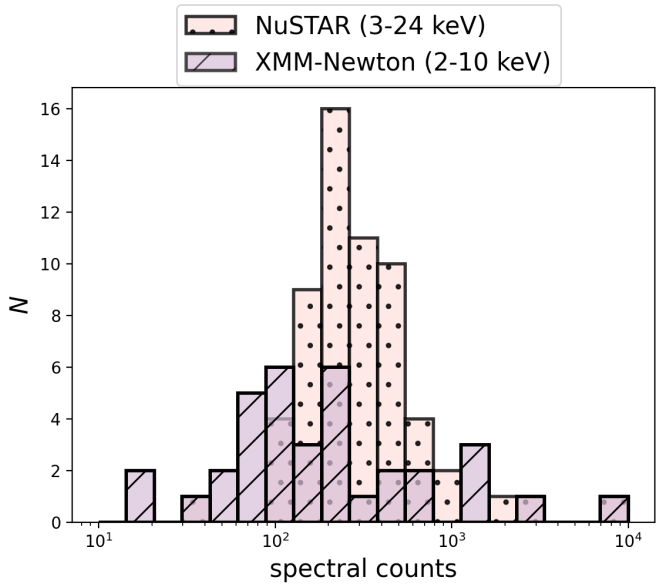

Figure 2. A histogram of the net spectral counts in NuSTAR (pink; dotted) and XMM-Newton (purple; hashed) for the sources in our sample.

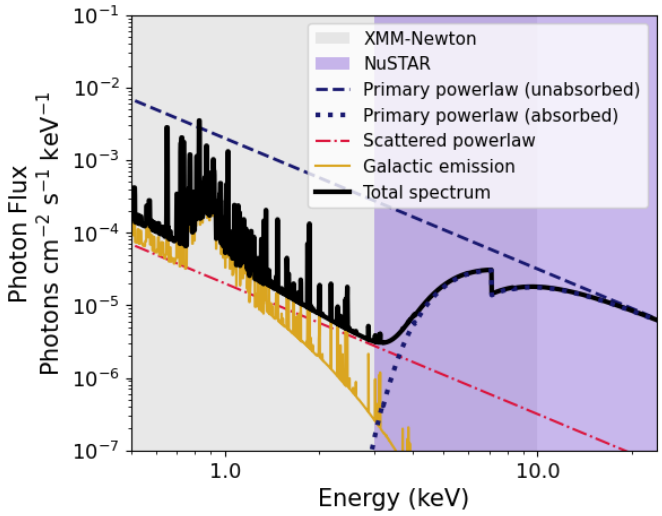

Figure 3. A schematic demonstrating the spectral components (unabsorbed (purple; dashed) and absorbed (purple; dotted) primary powerlaw, scattered powerlaw (red; dot-dashed), and galactic emission (gold; solid)) of the baseline model described in Section 3.2. This model is shown for a typical Compton Thin AGN with $N_{\rm H} = 10^{23}$ $\rm cm^{-2}$. The total spectrum is shown in bolded black. The background is shaded to demonstrate the energy range of XMM-Newton (gray) and NuSTAR (purple).

tered powerlaw, and galactic emission. Figure 3 shows a schematic of these components, and they are described in further detail below.

The transmitted powerlaw originates from the corona, which up-scatters UV and optical emission from the accretion disk into the X-ray band. Obscuring material along the line of sight suppresses soft X-rays, creating a low-energy cutoff whose location depends on $N_{\rm H}$.

The scattered powerlaw accounts for coronal emission that is Thomson scattered by warm photoionized material in the circumnuclear region (Matt & Iwasawa 2019). The parameters for the transmitted and scattered emission are equivalent, and the strength of the scattered component is controlled by a constant ($f_{\rm SCATT}$) that is free to vary between 10^{-5} and 0.1 (Buchner et al. 2019; Gupta et al. 2021).

A MEKAL component (Mewe et al. 1985, 1986; Liedahl et al. 1995) is commonly used to account for the < 3 keV emission of hot, diffuse gas within the host galaxy (e.g, Mineo et al. 2012; Torres-Albà et al. 2021; Silver et al. 2022; Diaz et al. 2023; Torres-Albà et al. 2023). We refer to this as the galactic component. We keep all parameters frozen except for the normalization ($n_{\rm gal}$), fixing the

temperature to $kT = 0.6$ keV (Gierliński & Done 2004), the hydrogen density to 1 cm^{-3}, and abundance to solar (1.0; Crummy et al. 2006). The redshift is that of the host galaxy, and the switch parameter is set to 1, meaning that the spectrum is interpolated from a pre-existing table.

Many AGN models also include a reflected component, which models X-rays that are reprocessed by circumnuclear material in the accretion disk and torus. This component creates a "Compton hump" at ~ 30 keV (rest frame) for obscured AGN and has negligible effects below those energies (see Figure 3 of Carroll et al. 2023) aside from an Fe Kα florescence line. All data are ignored above 24 keV and the SNR of the X-ray spectra in this work are generally too low to detect the Fe Kα line, so a separate reflected component would not be well constrained. However, one of our two models (Section 3.2) self-consistently includes reflected emission without requiring additional free parameters.

3.2. *The Models*

We employ two models for our fitting: a simplified "baseline" model that represents AGN as an obscured powerlaw, and a physically motivated torus model that more accurately reproduces the spectra of obscured AGN. While the baseline model is sufficient for unobscured sources, torus models self-consistently account for photoelectric absorption alongside Compton scattering, cold reflection, and florescent emission, all of which are negligible for unabsorbed AGN but become important at $\log(N_H) \gtrsim 23$ (Yaqoob 2012; Baloković et al. 2018; Buchner et al. 2019). Therefore, the torus models gives a more accurate representation of the parameter space for these C-Thin and CT sources. When interpreting results (Section 4), we follow Zappacosta et al. (2018) by employing the baseline model for sources with $\log(N_H) < 23$ and the clumpy torus model for $\log(N_H) \geq 23$.

The baseline model is defined as follows:

$$\begin{aligned} &\text{PHABS}_{\text{GAL}} * (\text{ZPHABS}_{\text{TOR}} * \text{ZPOWERLW} + \\ &\qquad f_{\text{SCATT}} * \text{ZPOWERLW} + \text{MEKAL}). \end{aligned} \tag{1}$$

The baseline model has two absorption components (PHABS): one for Galactic absorption from the Milky Way (Dickey & Lockman 1990; Kalberla et al. 2005; HI4PI Collaboration et al. 2016), and another representing intrinsic absorption from the AGN torus or host galaxy ($N_{\rm H}$). The corona is modeled by a redshifted powerlaw (ZPOWERLW), which has two free parameters: the photon index (Γ hereafter) and the normalization. The strength of the scattered powerlaw is controlled by a constant ($f_{\rm SCATT}$). The galactic emission is represented by MEKAL.

The second model used to describe the X-ray spectra employs the UXCLUMPY torus model by Buchner et al. (2019), which is widely used for analyzing obscured AGN (i.e. Marchesi et al. 2022; Torres-Albà et al. 2023; Akylas et al. 2024; Boorman et al. 2025; Torres-Albà et al. 2025). This model follows the formalism of the CLUMPY model for IR emission Nenkova et al. (2008a,b), which describes the dusty torus as a gaussian distribution of clouds with various column densities. UXCLUMPY was designed to match the frequency of eclipsing events observed by Markowitz et al. (2014) and the $N_{\rm H}$ distribution measured by Aird et al. (2015), Buchner et al. (2015), and Ricci et al. (2015). We hereafter refer to this as the clumpy model:

$$\begin{aligned} &\text{PHABS} * (\text{UXCLUMPY-CUTOFF} + f_{\text{SCATT}} * \\ &\qquad \text{UXCLUMPY-CUTOFF-OMNI} + \text{MEKAL}). \end{aligned} \tag{2}$$

In the clumpy model, the PHABS component represents absorption from the Milky Way. Absorption from obscuring material within the circumnuclear region ($N_{\rm H}$) is a free parameter of UXCLUMPY-CUTOFF, which self-consistently models the transmitted and reflected X-ray emission from a clumpy torus surrounding the central engine. UXCLUMPY-CUTOFF-OMNI represents the scattered component, which is modeled as the transmitted powerlaw scattered by warm material beyond the influence of the obscuring torus. Just as with the baseline model, the strength of the scattered component is controlled by a constant $f_{\rm SCATT}$. Galactic emission is represented by a MEKAL component.

As is standard for analysis of faint sources, torus parameters are kept fixed to average values. The only UXCLUMPY parameters kept free are $N_{\rm H}$, Γ, and the powerlaw normalization. The high energy cutoff is set to 400 keV (Baloković et al. 2020). The parameters TORSigma and CTKcover—which together describe the covering fraction of the obscuring material—have minor effects on the spectra in the 0.1-24 keV energy range, so we fix them to median values (45 and 0.4, respectively). The inclination angle ($\Theta_{\rm inc}$) is set to 90.0°, which represents an edge-on AGN. Following unification schemes (Antonucci 1993; Urry & Padovani 1995; Ricci et al. 2017), unobscured AGN have lower $\Theta_{\rm inc}$. However, this parameter has negligible effects on the fits, so we keep it fixed throughout the process.

For both models, the redshift is that of the host galaxy. Sources without multi-wavelength counterparts are assigned $z = 0.5$, which is the median redshift of the sample.

3.3. *Fitting Procedure*

To begin the fitting procedure, we first determined whether to employ scattered powerlaw or galactic emission components. If there are no XMM-Newton data for a source, both components are excluded. Where XMM-Newton spectra exist, low signal-to-noise in the soft end leads to degeneracy between the galactic emission and the scattered component. As a result, we chose to use one of the two components based on whichever best improves the fit by minimizing the Cash statistic (C; Cash 1979). In cases where neither the scattered nor galactic components improved the fit by a significant amount, both were excluded. In order to be considered a significant improvement, the C statistic must decrease by more than the change in the degrees of freedom.

Once the model components were chosen for each source, parameter values were obtained using the Bayesian X-ray Analysis (BXA) package (Buchner et al. 2014). BXA utilizes UltraNest[4]—a Bayesian nested sampling package by Buchner (2021)—to thoroughly search the parameter space. This careful statistical treatment is necessary to avoid falling in local minima, which the standard XSPEC fitting routines are prone to do, especially in the complex parameter spaces created by physically realistic torus models. BXA produces a posterior distribution which contains probability distribution functions (PDFs) for all free parameters. Below, we describe the priors used for fitting the free parameters.

Where the baseline and clumpy models share the same free parameters, we adopt the same priors for both. $N_{\rm H}$ is assigned a log-uniform prior between 1.0×10^{20} cm^{-2} and 1.0×10^{26} cm^{-2}. Γ is assigned a Gaussian prior centered at 1.8—which is the average value for AGN (e.g. Nandra & Pounds 1994; Ricci et al. 2017)—with a standard deviation of $\lambda = 0.15$. For the clumpy model, a log-uniform prior is used for the powerlaw normalization (min $= 10^{-10}$, max $= 0.1$). For the baseline model, we instead keep the powerlaw normalization fixed and use a CFLUX component, which calculates the flux of the given component (in this case, the 2-10 keV flux of the transmitted powerlaw). This enables the unabsorbed flux and luminosity to be directly measured. The CFLUX parameter is already in log space, so it is assigned a uniform prior between -15 and -10. If a galactic or scattered component is included for a source, a log-uniform prior is assigned for $f_{\rm SCATT}$ (min $= 10^{-5}$, max $= 0.1$) or $n_{\rm GAL}$ (min $= 10^{-10}$, max $= 0.1$), respectively.

[4] https://johannesbuchner.github.io/UltraNest/

As a supplement to the BXA results, frequentist best-fit models were obtained using the standard routines in HEASOFT's PyXSPEC. Fits are found using a semi-automated routine, which is described below.

The process for fitting the baseline model begins by freezing $N_{\rm H}$ to a negligible value, then constraining Γ and the normalization of the transmitted powerlaw spectrum. Γ is then frozen to the best-fit value, and constraints are found on $N_{\rm H}$. Lastly, Γ is freed in order to fit both Γ and $N_{\rm H}$ to the spectrum. For cases where Γ is unconstrained or unrealistically low for an AGN ($\Gamma < 1.5$), it is fixed to 1.8 and constraints on $N_{\rm H}$ are obtained.

We employ a slightly different fitting routine for the clumpy model. The method follows the suggestion of Buchner et al. (2019) by first fitting the clumpy model to the hard-band data (20-24 keV) with Γ, $N_{\rm H}$, and the normalization as free parameters. This focuses on fitting the intrinsic powerlaw and avoids hitting deep local minima in the parameter space. After obtaining initial constraints on $N_{\rm H}$ and Γ, the energy range is increased gradually (down to 15 keV, 8 keV, 5 keV, then all the data), and re-fit until the full NuSTAR (3-24 keV) and XMM-Newton (0.1-10 keV) bands are included. If $\Gamma < 1.5$, this process is repeated with Γ frozen to 1.8, then Γ is freed in the final step. In the case that Γ is still unrealistically low, we retain the model with $\Gamma = 1.8$.

For both the baseline and clumpy models, the final step of the automated routine is to fold in either the reflection component or the galactic emission, if either was used in the BXA fitting. Manual inspection allowed for direct comparison between parameter values of the two models. Where discrepancies emerged, the source of the discrepancy was identified and the model was manually re-fit. At the end of this process, the baseline and clumpy models yield consistent $N_{\rm H}$ values, as demonstrated by Figure 4 (AGN 29, which has $N_{\rm H} \lesssim 10^{19}$ for both models, has been excluded from this plot for clarity).

More detail about individual fits—including the BXA results and frequentist best-fit parameters for each AGN—are shown in Appendix B.

4. RESULTS

For the following discussion, two objects (ID 3 and 18) have been excluded. ID 3 was identified as a star by Z24, and a trustworthy fit could not be found for AGN 18 (as described in Appendix B).

4.1. *Observed $N_{\rm H}$ Distribution*

In order to have a careful statistical treatment of our analysis, we chose to use the Bayesian results for calculating the $N_{\rm H}$ distribution of the sample. Following

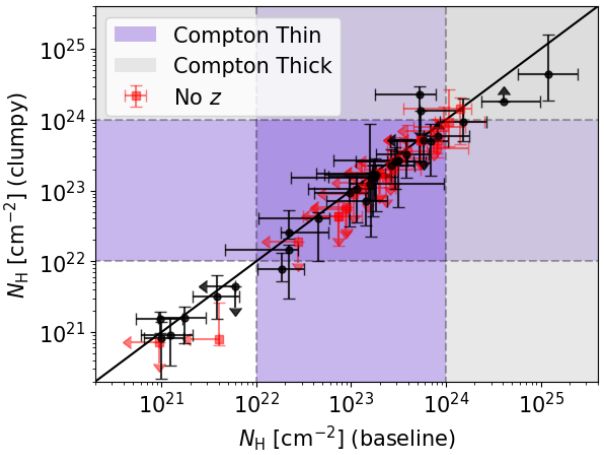

Figure 4. A comparison of the best-fit column densities ($N_{\rm H}$) for the baseline and clumpy models. The shaded regions mark the Compton Thin (purple) and Compton Thick (gray) regimes. Sources without redshift measurements are shown as red squares.

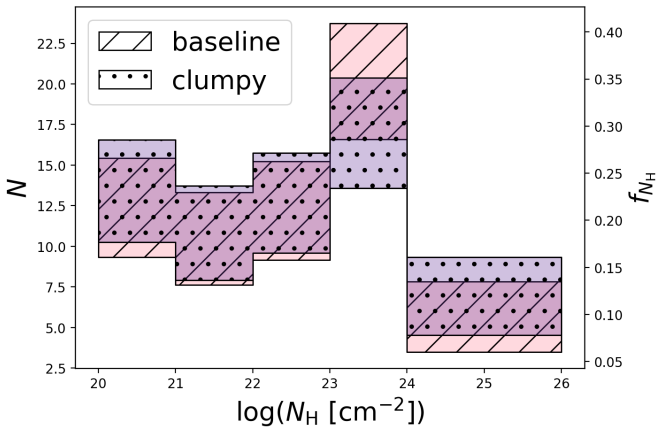

Figure 5. The effective number N and fraction $f_{N_{\rm H}}$ of AGN observed in each log($N_{\rm H}$) bin within 1σ for the baseline (pink; hatched) and clumpy (purple; dotted) models, as derived by integrating the summed PDF shown in Figure 13 (Appendix B).

the methodology presented by Lanzuisi et al. (2018), the observed $N_{\rm H}$ distribution is found by extracting the posteriors produced by BXA (Section 3.3). Smoothed PDFs were created for each source by applying a Gaussian Kernel Density Estimator (KDE; bandwith = 0.01) to $N_{\rm H}$ and normalizing so that the total integral of the curve is equal to 1. Adding the PDFs from all sources then yields the observed $N_{\rm H}$ distribution of the sample. Figure 12 in Appendix B shows the individual PDFs of each source, and Figure 13 shows the summed PDF of the sample.

The sample is then divided into 1 dex log($N_{\rm H}$ [cm^{-2}]/cm^{-2}) (log($N_{\rm H}$) for brevity) bins, with

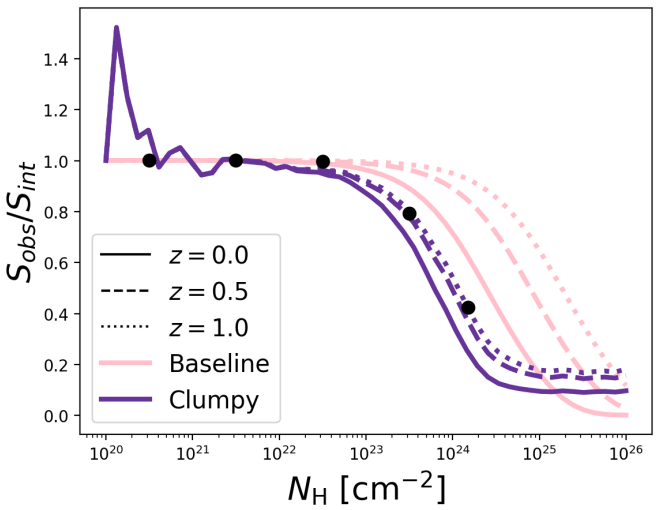

Figure 6. The ratio of observed to absorption-corrected 8-24 keV flux ($S_{\rm obs}/S_{\rm int}$) as a function of absorption. The flux ratios are shown for the clumpy (purple) and baseline (pink) models at z = 0.0 (solid lines), 0.5 (dashed lines), and 1.0 (dotted lines). The black points denote the ratios used in Equation 4 for each log($N_{\rm H}$) bin (see Table 4).

one bin representing the CT regime (log($N_{\rm H}$) > 24). To estimate the number N and fraction $f_{N_{\rm H}}$ of AGN in each bin, the summed PDF is integrated within the bin. 1σ confidence intervals are calculated using the process outlined by Cameron (2011), which uses the beta distribution to estimate confidence intervals on binomial population proportions (see Appendix A of Cameron 2011), where the number of successes is defined as the effective sample within the bin (N), and the sample size is the number of AGN used in the analysis (58). This process gives estimates for observed $f_{\text{C-Thin}}$ (fraction of sources with $N_{\rm H} > 10^{22}$ cm^{-2}) and f_{CT}. For the baseline/clumpy model, this yields $f_{\text{C-Thin}}$ of $0.54^{+0.06}_{-0.06}/0.49^{+0.06}_{-0.06}$ and $f_{\rm CT} = 0.09^{+0.02}_{-0.05}/0.11^{+0.03}_{-0.05}$.

4.2. *Intrinsic $N_{\rm H}$ Distribution*

Even with NuSTAR's hard energy range, intrinsically faint AGN become more difficult to detect in the CT regime due to emission being heavily attenuated (e.g. Burlon et al. 2011); as shown in Figure 6, much of the X-ray emission in the 8-24 keV band is suppressed at high absorption. In order to account for this absorption bias, we follow the process outlined by Burlon et al. (2011) and Zappacosta et al. (2018) and derive an estimate of the true, intrinsic $N_{\rm H}$ ($dN/d\log N_{\rm H}$) distribution by binning the sample into log($N_{\rm H}$) bins and integrating the log$N$-log$S$ relation (dN/dS) of each bin over an appropriate flux range:

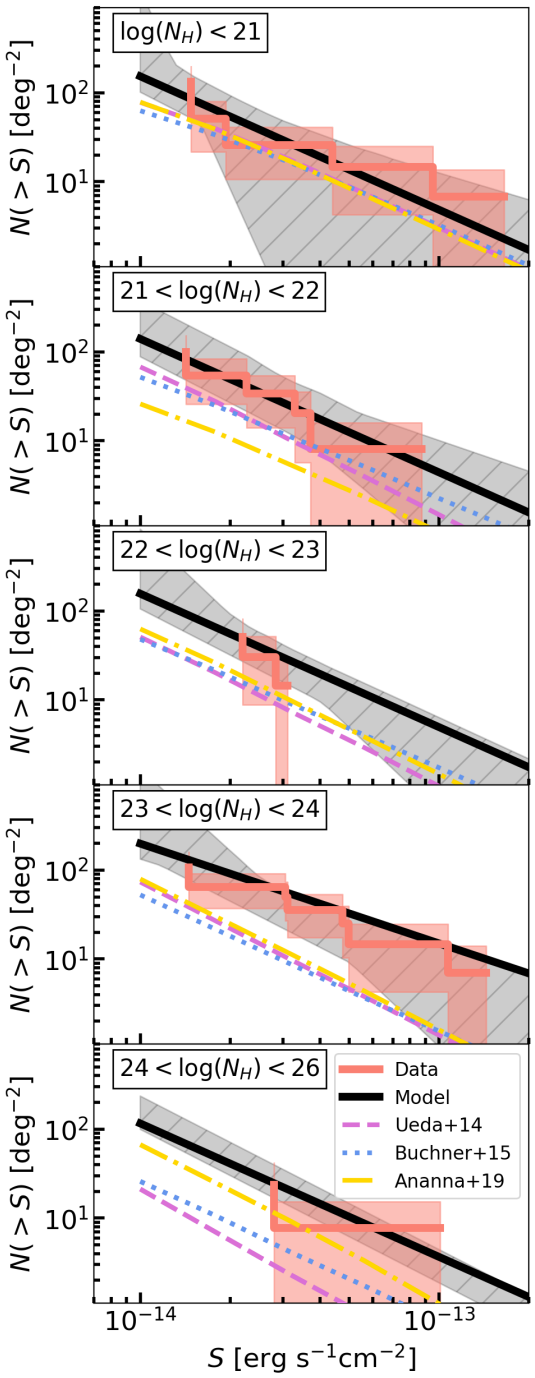

Figure 7. The median 8-24 keV logN-logS models (black lines) and 3σ confidence intervals (hatched regions) are shown in each $\log(N_{\rm H})$ bin over 1000 iterations of the sample, as described in Section 4.2. The nominal data (binned using the median $N_{\rm H}$ from the posterior) are plotted in solid pink with poisson error bars (shaded region). logN-logS relations from population synthesis models (Ueda et al. 2014; Buchner et al. 2015; Ananna et al. 2019) are shown for comparison.

$$\frac{dN}{d\log N_{\rm H}} = \int_{S^{\rm obs}_{\rm min}}^{S^{\rm obs}_{\rm max}} \frac{dN}{dS}\, dS. \tag{3}$$

This analysis is performed in the $8-24$ keV band. Only sources detected above the 95% reliability threshold and with signal to noise ratios > 2.5 are used in order to ensure accurate log$N$-log$S$ modeling. This reduces the sample to 24 objects (see Table 7 in Appendix B and Table 2 in Z24). In the following steps, we describe our procedure for acquiring the parameters in Equation 3.

The first step is to select 1000 random realizations from the posteriors produced by BXA. The clumpy model results are only used for objects whose clumpy and baseline posteriors are both $\geq 90\%$ above $\log(N_{\rm H}) = 23$. Beyond this threshold, the physically motivated components of obscured AGN become significant (Yaqoob 2012; Baloković et al. 2018; Buchner et al. 2019). The clumpy model is unnecessarily complex for less obscured spectra, so all other sources are assigned their baseline posteriors.

For each realization, we divide the sample into 1 dex $\log(N_{\rm H})$ bins, create cumulative flux distributions (log$N$-log$S$) per bin, and fit the log$N$-log$S$ curves to powerlaw functions $(N(>S) = A(N_{\rm H})S^{-\alpha}$, where α is the powerlaw slope and $A(N_{\rm H})$ is the normalization at 10^{13} erg/s/cm^2). The slope for a Euclidean universe ($\alpha = 3/2$) is assumed for bins with < 5 sources.

Each $\log(N_{\rm H})$ bin is assigned the median $A(N_{\rm H})$ and α from the 1000 realizations. In Figure 7, these median logN-logS models are plotted alongside the data (which are assigned the median $N_{\rm H}$ from their posterior distribution) and compared to Ueda et al. (2014), Buchner et al. (2015), and Ananna et al. (2019). In each $\log(N_{\rm H})$ bin, we find $\gtrsim 2$ times more sources than are predicted by these population synthesis models, which is consistent with the logN-logS curve of the 8-24 keV sample as a whole (see the middle panel of Figure 20 in Z24).

Before performing the integral in Equation 3, the flux range must be carefully selected. In particular, minimum observed fluxes ($S^{\rm obs}_{\rm min}$) must be chosen so that the intrinsic (absorption-corrected) flux $S^{\rm int}_{\rm min}$ is the same in each $\log(N_{\rm H})$ bin. That way, we can be relatively confident that all AGN down to $S^{\rm int}_{\rm min}$ are being detected regardless of $N_{\rm H}$.

To select $S^{\rm int}_{\rm min}$, we start by finding the minimum observed flux that appears in the CT bin ($\log(N_{\rm H}) > 24$). The CT bin for this sample is sensitive down to $S_{\rm obs} \approx 3.0 \times 10^{-14}$ erg/s/cm^2, which corresponds to an unabsorbed flux of $S_{\rm int} \approx 6.0 \times 10^{-14}$ erg/s/cm^2, so this becomes $S^{\rm int}_{\rm min}$. In each $N_{\rm H}$ bin, this is converted to an observed flux $S^{\rm obs}_{\rm min} = k(N_{\rm H})S^{\rm int}_{\rm min}$, where $k(N_{\rm H})$ is pulled

Table 4. Best-fit logN-logS parameters. The normalization is defined as the value at 10^{-13} ($A(N_{\rm H}) = N(> S(3-24\ {\rm keV}) = 10^{-13}\ {\rm erg/s/cm^2})$)

$\log(N_{\rm H})$	$< z >$	α	$A(N_{\rm H})$	$k(N_{\rm H})$
20-21	0.65	$1.50^{+5.0}_{-0.6}$	5.2^{+11}_{-5}	1.00
21-22	0.58	$1.50^{+0.9}_{-0.5}$	4.5^{+10}_{-3}	1.00
22-23	0.57	$1.50^{+1.3}_{-0.2}$	5.1^{+5}_{-4}	1.00
23-24	0.62	$1.12^{+1.5}_{-0.3}$	12.5^{+8}_{-10}	0.79
24-26	0.86	$1.50^{+0.0}_{-0.0}$	3.7^{+4}_{-1}	0.42

from $S_{\rm obs}/S_{\rm int}$ curves shown in Figure 6. For our chosen value of $\Theta_{\rm inc}$, the $k(N_{\rm H})$ of UXCLUMPY behaves erratically at $\log(N_{\rm H}) < 23$ (Figure 6). Since we only use the clumpy model for $\log(N_{\rm H}) > 23$, this does not affect our analysis.

In order to compute $k(N_{\rm H})$, $\log(N_{\rm H})$ is set to the middle of each bin. However, the CT bin has a large range of $k(N_{\rm H})$, so we chose to calculate $k(N_{\rm H})$ at $N_{\rm H} = 1.5 \times 10^{24}$ cm^{-2}, which is the formal definition of the CT threshold and gives a conservative estimate of f_{CT} (as done by Zappacosta et al. 2018). A scattered component with $f_{scatt} = 10.9 \times N_{\rm H}^{-0.47}$ is assumed (see Table 1 from Gupta et al. 2021), and the redshift is set to the median redshift of objects in that bin.

Table 4 reports the median redshifts, $k(N_{\rm H})$, and logN-logS parameter values. These parameters go into Equation 3 after performing the integral:

$$\frac{dN}{d\log N_{\rm H}} = \frac{A(N_{\rm H})}{(10^{-13})^{-\alpha}} \left[(S^{\rm obs}_{\rm max})^{-\alpha} - (S^{\rm obs}_{\rm min} k(N_{\rm H}))^{-\alpha} \right]. \quad (4)$$

Figure 8 shows the resulting measurement of the intrinsic $N_{\rm H}$ distribution alongside all 1000 realizations of the sample. Correcting for absorption bias and using a minimum unabsorbed flux of $S^{int}_{min} = 6.0 \times 10^{-14}$ erg/s/cm^2 yields $f_{CT} = 0.30^{+0.23}_{-0.08}$. For comparison, the $N_{\rm H}$ distribution is also shown without accounting for absorption bias, but using the same flux limit. This gives $f_{CT} = 0.13^{+0.15}_{-0.04}$.

5. DISCUSSION

5.1. *Comparison to previous measurements*

In every column density bin, we find more sources than are expected from population synthesis models (Ueda et al. 2014; Buchner et al. 2015; Ananna et al. 2019, see Figure 7). However, our observed f_{CT} is consistent with Ananna et al. (2019) (Figure 8). Table 5 compares our absorption-corrected calculation of f_{CT} to measurements found in previous surveys (Wilkes et al. 2013; Civano et al. 2015; Lanzuisi et al. 2018; Masini et al. 2018; Zappacosta et al. 2018; Kuraszkiewicz et al. 2021; Torres-Albà et al. 2021; Carroll et al. 2023; Akylas et al. 2024; Boorman et al. 2025), and the latest population synthesis models (Ananna et al. 2019; Gerolymatou et al. 2025). In all cases, the measurements reported in Table 5 use $f_{CT} = N_{CT}/N_{\rm total}$, where Wilkes et al. (2013) and Kuraszkiewicz et al. (2021) use 1.5×10^{24} cm^2 as their CT threshold and all other studies (including this work) use 10^{24} cm^2. Our finding is consistent with these previous studies, though with large errorbars. The luminosity distributions of these studies are also listed. For this work, the intrinsic (unabsorbed) 2-10 keV luminosity distribution of sources with redshift measurements is shown in Figure 9.

Future work could improve this measurement by including the full Cycle 5+6+8+9 catalog (Silver et al. 2025) and XMM-Newton identified sources. Additionally, the measured value of f_{CT} can vary dramatically based on the model used (Boorman et al. 2025), and incorporating a larger variety of models would yield a more robust measurement of f_{CT}.

Some unusual features appear in the $\log(N_{\rm H})$ distribution. In particular, we find a small fraction ($\sim 20\%$) of AGN in the $\log(N_{\rm H}/{\rm cm}^{-2}) = 20-21$ bin, which conflicts with most of the studies shown in Table 5 and Figure 8. Additionally, the distribution is relatively flat at $\log(N_{\rm H}) < 23$. This may be due to the lack of XMM-Newton matches for many objects. Without XMM-Newton, the degree of obscuration is difficult to constrain at low values, leading to flat PDFs (see Figure 12 in Appendix B).

In order to derive the relationship between f_{CT} and the observed 8-24 keV flux, f_{CT} and 3σ confidence intervals were calculated for different values of S^{obs}_{8-24} using the logN-logS models in Figure 7. Figure 10 shows the results compared to population synthesis models up to $z > 3$ (Ueda et al. 2014; Aird et al. 2015; Buchner et al. 2015; Ananna et al. 2019) and previous measurements from the NuSTAR COSMOS (Civano et al. 2015) and UDS (Masini et al. 2018) surveys. Within uncertainties, the data are consistent with Buchner et al. (2015) and Ananna et al. (2019).

5.2. *Redshift evolution*

As discussed in Section 2.3, 33 of the sources in this work have multi-wavelength matches with redshift measurements. While this sample is incomplete, there are enough sources to perform a preliminary test of previous studies (Lanzuisi et al. 2018; Peca et al. 2023), which find that obscured AGN dominate at higher redshifts.

After splitting the sample into low ($z < 1$) and high ($z > 1$) redshift bins, we use the same method described

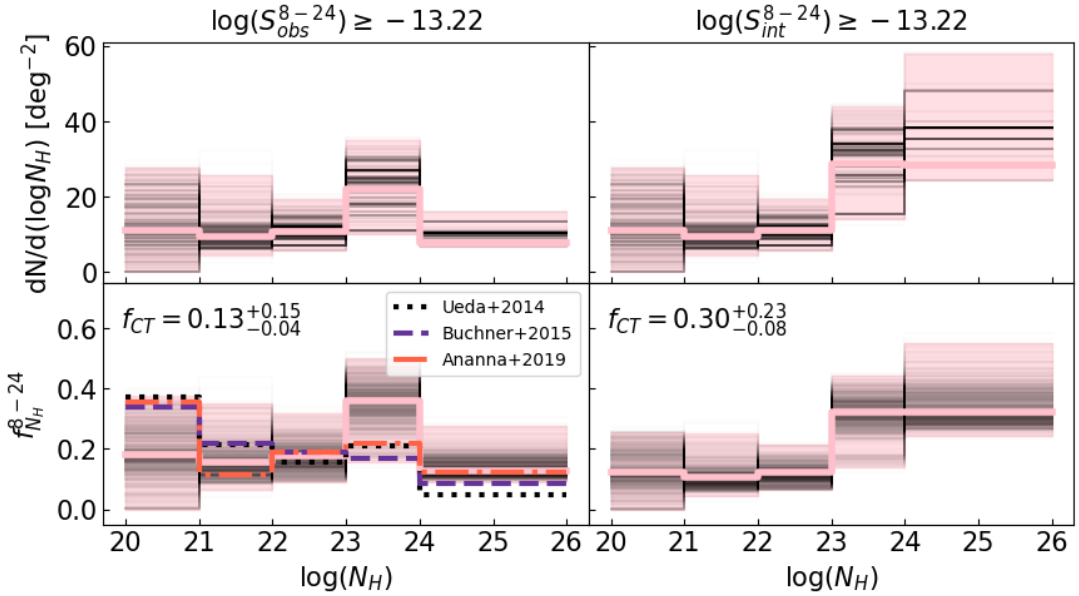

Figure 8. The $N_{\rm H}$ distribution (top) and $N_{\rm H}$ fraction (bottom) of the sample down to an observed (left) and absorption-corrected (right) 8-24 keV flux of 6.0×10^{-14} erg/s/cm^2. The distribution has been calculated over 1000 realizations, all plotted in black, and the median and 3σ errors of the distribution are plotted in pink. The predicted observed $f_{N_{\rm H}}$ for our sample is shown for three population synthesis models (Ueda et al. 2014; Buchner et al. 2015; Ananna et al. 2019) in the bottom-left figure.

Table 5. Measurements of f_{CT}

Work	z	L_X [a]	f_{CT}
Ananna+ 19	≤ 1	$10^{41} < L^{int}_{2-10} < 10^{47}$	0.56 ± 0.07
Gerolymatou+ 25	≤ 3	$10^{41.5} < L^{int}_{2-10} < 10^{46.5}$	0.21 ± 0.07
Wilkes+ 13	$1.0 - 2.0$	$10^{43} < L^{int}_{2-8} < 10^{45.75}$	0.21 ± 0.07
Civano+ 15	~ 0.5	$10^{42} < L^{obs}_{10-40} < 10^{45.5}$	0.13 ± 0.03
Lanzuisi+ 18	$0.1 - 1$	$10^{41.5} < L^{int}_{2-10} < 10^{45.5}$	~ 0.2
	$1 - 2$		~ 0.3
	$2 - 3$		~ 0.5
Zappacosta+ 18	~ 0.5	$10^{42.6} < L^{int}_{10-40} < 10^{45.6}$	0.02-0.56
Masini+ 18	~ 1	$10^{42.1} < L^{obs}_{10-40} < 10^{46}$	0.115 ± 0.020
Kuraszkiewicz+ 21	$0.5 - 1.0$	$10^{41} < L^{int}_{2-10} < 10^{47}$	~ 0.2
Torres-Albà+ 21	≤ 0.05	$10^{42} \lesssim L^{int}_{2-10} \lesssim 10^{44}$	~ 0.08
Carroll+ 23	≤ 0.8	$10^{42.5} < L^{int}_{2-10} < 10^{44.7}$	$0.555^{+0.037}_{-0.032}$
Akylas+ 24	< 0.02	$10^{39.5} < L^{int}_{2-10} < 10^{44.5}$ [b]	0.25 ± 0.05
Boorman+ 25	≤ 0.044	$10^{41} \lesssim L^{int}_{2-10} \lesssim 10^{44}$	0.35 ± 0.09
This work	~ 0.5	$10^{42} \lesssim L^{int}_{2-10} \lesssim 10^{46}$	$0.30^{+0.21}_{-0.08}$

[a] X-ray Luminosity distribution reported by the study in units of erg s^{-1}. Superscripts indicate the energy band (in keV) and subscripts define whether the reported luminosities are observed or intrinsic (corrected for absorption).
[b] Only the luminosities of sources detected in the X-ray are reported.

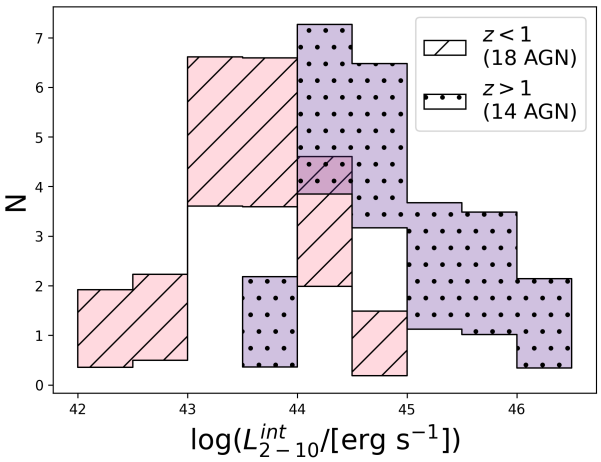

Figure 9. The unabsorbed 2-10 keV luminosity distribution of sources with redshift measurements. The sample is split into low ($z < 1$; pink, hatched) and high ($z > 1$; purple, dotted) redshift bins. The shaded region gives 1σ confidence intervals.

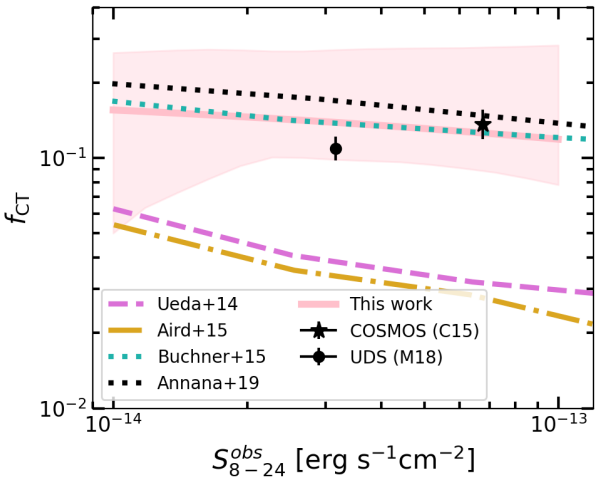

Figure 10. f_{CT} as a function of observed 8-24 keV flux (solid pink), with the shaded region denoting 3σ error bars for this work. For comparison, predictions from population synthesis models ($z < 3$; Ueda et al. 2014; Aird et al. 2015; Buchner et al. 2015; Ananna et al. 2019) and f_{CT} measurements from the NuSTAR COSMOS (Civano et al. 2015, black star) and UDS (Masini et al. 2018, black dot) surveys are shown.

in Section 4.1—using the baseline model for sources with $N_{\rm H} < 23$ and the clumpy model for $N_{\rm H} \geq 23$—to derive the observed $N_{\rm H}$ distribution shown in Figure 11. A two sample KS test is used to assess whether the low and high redshift samples are significantly different. Iterating over 1000 realizations of the sample drawn from the posteriors (as described in Section 4.2) and performing the KS test in each realization yields an average p-value of 0.023. This p-value suggests that the samples

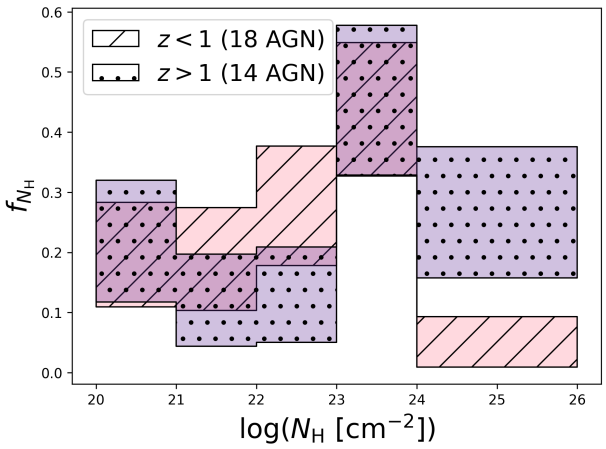

Figure 11. The observed column density distribution of the sample for low ($z < 1$; pink, hashed) and high ($z > 1$; purple, dotted) redshifts.

are statistically different, with more CT objects falling in the $z > 1$ bin. We observe $f_{CT} < 0.09$ for the low redshift sample and $f_{CT} = 0.23^{+0.14}_{-0.08}$ for the $z > 1$ sample. However, this does not account for luminosity and redshift-dependent biases. Accounting for these biases is non-trivial (i.e, see Peca et al. 2023), and we leave it to future work as spectroscopic campaigns yield a more complete sample of redshifts.

6. SUMMARY AND CONCLUSIONS

We derive the $N_{\rm H}$ distribution of the hard X-ray detected sources identified in the Z24 NuSTAR-NEP catalog. We use two models—a baseline absorbed power-law model and a clumpy torus model (Buchner et al. 2019)— and we employ a Bayesian treatment (Buchner et al. 2014) to fully encapsulate the complicated parameter spaces of our models. We summarize our findings below.

- We measure a Compton Thick fraction of $0.13^{+0.15}_{-0.04}/0.30^{+0.21}_{-0.08}$ down to an observed/unabsorbed flux of 6.0×10^{-14} erg/s/cm^2 (see Figure 8 and Table 5).
- Our Compton Thick fraction is consistent with population synthesis models and previous studies (see Table 5 and Figure 8), though we find a flatter $N_{\rm H}$ distribution for unabsorbed sources. This may be explained by poor statistics, especially in the soft band for sources without XMM-Newton counterparts. Additionally, we are likely underestimating the $N_{\rm H}$ of the 27 sources that lack redshift measurements.
- The measured relationship between f_{CT} and the observed 8-24 keV flux is consistent with previous

findings (Buchner et al. 2015; Civano et al. 2015; Masini et al. 2018; Ananna et al. 2019), though with large uncertainties.

- From the 33 sources with redshift measurements, we see evidence that the $N_{\rm H}$ distribution may evolve with redshift, with an observed CT fraction $f_{CT} < 0.09$ for low redshift sources ($z < 1$) and $f_{CT} = 0.23^{+0.14}_{-0.08}$ for high-redshift sources ($z > 1$). More complete redshift measurements and a thorough account of redshift and luminosity-dependent biases are needed to investigate this finding.

The NEP field has some of the deepest X-ray data available, and it is the only deep survey designed to have simultaneous soft and hard X-ray observations. However, this type of simultaneous program is resource-intensive, and observational constraints on faint AGN in the NEP field come with large uncertainties. This demonstrates that a new telescope with high angular resolution and broad-band X-ray spectroscopy (such as the previously proposed X-ray probe-class mission HEX-P; Boorman et al. 2024; Civano et al. 2024; García et al. 2024; Kammoun et al. 2024; Pfeifle et al. 2024; Piotrowska et al. 2024) would be an invaluable asset to future studies of AGN in the X-ray band.

ACKNOWLEDGMENTS

The material is based upon work supported by NASA under award numbers 80GSFC21M0002 and 80NSSC24K1482. This work made use of data from the NuSTAR mission, which is led by the California Institute of Technology, managed by the Jet Propulsion Laboratory, and funded by the National Aeronautics and Space Administration. Additionally, this work made use of data from XMM-Newton, an ESA science mission with instruments and contributions directly funded by ESA Member States and NASA. CNAW acknowledges funding from JWST/NIRCam contract to the University of Arizona NAS5-02015.

This research used data obtained with the Dark Energy Spectroscopic Instrument (DESI). DESI construction and operations is managed by the Lawrence Berkeley National Laboratory. This material is based upon work supported by the U.S. Department of Energy, Office of Science, Office of High-Energy Physics, under Contract No. DE–AC02–05CH11231, and by the National Energy Research Scientific Computing Center, a DOE Office of Science User Facility under the same contract. Additional support for DESI was provided by the U.S. National Science Foundation (NSF), Division of Astronomical Sciences under Contract No. AST-0950945 to the NSF's National Optical-Infrared Astronomy Research Laboratory; the Science and Technology Facilities Council of the United Kingdom; the Gordon and Betty Moore Foundation; the Heising-Simons Foundation; the French Alternative Energies and Atomic Energy Commission (CEA); the National Council of Humanities, Science and Technology of Mexico (CONAHCYT); the Ministry of Science and Innovation of Spain (MICINN), and by the DESI Member Institutions: www.desi.lbl.gov/collaborating-institutions. The DESI collaboration is honored to be permitted to conduct scientific research on I'oligam Du'ag (Kitt Peak), a mountain with particular significance to the Tohono O'odham Nation. Any opinions, findings, and conclusions or recommendations expressed in this material are those of the author(s) and do not necessarily reflect the views of the U.S. National Science Foundation, the U.S. Department of Energy, or any of the listed funding agencies.

This work also made extensive use of Astropy (Astropy Collaboration et al. 2013; Price-Whelan et al. 2018; Astropy Collaboration et al. 2022), numpy (Harris et al. 2020), and SciPy (Virtanen et al. 2020). We would also like to thank the High Energy Astrophysics Science Archive Research Center (HEASARC) team; this work would not have been possible without their data and software.

We thank the anonymous referee for their comments, which greatly improved this paper. Lastly, we thank thank Steven Willner for his comments and and Luca Zappacosta for helpful discussion.

REFERENCES

Abdurro'uf, Accetta, K., Aerts, C., et al. 2022, ApJS, 259, 35, doi: 10.3847/1538-4365/ac4414

Aihara, H., Armstrong, R., Bickerton, S., et al. 2018, PASJ, 70, S8, doi: 10.1093/pasj/psx081

Aird, J., Coil, A. L., Georgakakis, A., et al. 2015, MNRAS, 451, 1892, doi: 10.1093/mnras/stv1062

Akylas, A., Georgantopoulos, I., Gandhi, P., Boorman, P., & Greenwell, C. L. 2024, A&A, 692, A250, doi: 10.1051/0004-6361/202451906

Alexander, D. M., Stern, D., Del Moro, A., et al. 2013, ApJ, 773, 125, doi: 10.1088/0004-637X/773/2/125

Ananna, T. T., Treister, E., Urry, C. M., et al. 2019, ApJ, 871, 240, doi: 10.3847/1538-4357/aafb77

Ananna, T. T., Weigel, A. K., Trakhtenbrot, B., et al. 2022, ApJS, 261, 9, doi: 10.3847/1538-4365/ac5b64
Antonucci, R. 1993, ARA&A, 31, 473, doi: 10.1146/annurev.aa.31.090193.002353
Astropy Collaboration, Robitaille, T. P., Tollerud, E. J., et al. 2013, A&A, 558, A33, doi: 10.1051/0004-6361/201322068
Astropy Collaboration, Price-Whelan, A. M., Lim, P. L., et al. 2022, ApJ, 935, 167, doi: 10.3847/1538-4357/ac7c74
Baloković, M., Brightman, M., Harrison, F. A., et al. 2018, ApJ, 854, 42, doi: 10.3847/1538-4357/aaa7eb
Baloković, M., Harrison, F. A., Madejski, G., et al. 2020, ApJ, 905, 41, doi: 10.3847/1538-4357/abc342
Boorman, P. G., Torres-Albà, N., Annuar, A., et al. 2024, Frontiers in Astronomy and Space Sciences, 11, 1335459, doi: 10.3389/fspas.2024.1335459
Boorman, P. G., Gandhi, P., Buchner, J., et al. 2025, ApJ, 978, 118, doi: 10.3847/1538-4357/ad8236
Boquien, M., Burgarella, D., Roehlly, Y., et al. 2019, A&A, 622, A103, doi: 10.1051/0004-6361/201834156
Brammer, G. B., van Dokkum, P. G., & Coppi, P. 2008, ApJ, 686, 1503, doi: 10.1086/591786
Brightman, M., & Nandra, K. 2011, MNRAS, 413, 1206, doi: 10.1111/j.1365-2966.2011.18207.x
Brunner, H., Cappelluti, N., Hasinger, G., et al. 2008, A&A, 479, 283, doi: 10.1051/0004-6361:20077687
Buchner, J. 2021, The Journal of Open Source Software, 6, 3001, doi: 10.21105/joss.03001
Buchner, J., Brightman, M., Nandra, K., Nikutta, R., & Bauer, F. E. 2019, A&A, 629, A16, doi: 10.1051/0004-6361/201834771
Buchner, J., Georgakakis, A., Nandra, K., et al. 2014, A&A, 564, A125, doi: 10.1051/0004-6361/201322971
—. 2015, ApJ, 802, 89, doi: 10.1088/0004-637X/802/2/89
Burlon, D., Ajello, M., Greiner, J., et al. 2011, ApJ, 728, 58, doi: 10.1088/0004-637X/728/1/58
Cameron, E. 2011, PASA, 28, 128, doi: 10.1071/AS10046
Cappelluti, N., Brusa, M., Hasinger, G., et al. 2009, A&A, 497, 635, doi: 10.1051/0004-6361/200810794
Carroll, C. M., Ananna, T. T., Hickox, R. C., et al. 2023, ApJ, 950, 127, doi: 10.3847/1538-4357/acc402
Cash, W. 1979, ApJ, 228, 939, doi: 10.1086/156922
Ciesla, L., Charmandaris, V., Georgakakis, A., et al. 2015, A&A, 576, A10, doi: 10.1051/0004-6361/201425252
Civano, F., Hickox, R. C., Puccetti, S., et al. 2015, ApJ, 808, 185, doi: 10.1088/0004-637X/808/2/185
Civano, F., Zhao, X., Boorman, P. G., et al. 2024, Frontiers in Astronomy and Space Sciences, 11, 1340719, doi: 10.3389/fspas.2024.1340719
Comastri, A., Setti, G., Zamorani, G., & Hasinger, G. 1995, A&A, 296, 1, doi: 10.48550/arXiv.astro-ph/9409067
Crummy, J., Fabian, A. C., Gallo, L., & Ross, R. R. 2006, MNRAS, 365, 1067, doi: 10.1111/j.1365-2966.2005.09844.x
DESI Collaboration, Abdul-Karim, M., Adame, A. G., et al. 2025, arXiv e-prints, arXiv:2503.14745, doi: 10.48550/arXiv.2503.14745
Diaz, Y., Hernàndez-García, L., Arévalo, P., et al. 2023, A&A, 669, A114, doi: 10.1051/0004-6361/202244678
Dickey, J. M., & Lockman, F. J. 1990, ARA&A, 28, 215, doi: 10.1146/annurev.aa.28.090190.001243
Fabian, A. C., Zoghbi, A., Ross, R. R., et al. 2009, Nature, 459, 540, doi: 10.1038/nature08007
Ferrarese, L., & Merritt, D. 2000, ApJL, 539, L9, doi: 10.1086/312838
García, J. A., Stern, D., Madsen, K., et al. 2024, Frontiers in Astronomy and Space Sciences, 11, 1471585, doi: 10.3389/fspas.2024.1471585
Gebhardt, K., Bender, R., Bower, G., et al. 2000, ApJL, 539, L13, doi: 10.1086/312840
Gerolymatou, D., Paltani, S., Ricci, C., & Regamey, M. 2025, arXiv e-prints, arXiv:2506.14885, doi: 10.48550/arXiv.2506.14885
Gierliński, M., & Done, C. 2004, MNRAS, 349, L7, doi: 10.1111/j.1365-2966.2004.07687.x
Gilli, R., Comastri, A., & Hasinger, G. 2007, A&A, 463, 79, doi: 10.1051/0004-6361:20066334
Gupta, K. K., Ricci, C., Tortosa, A., et al. 2021, MNRAS, 504, 428, doi: 10.1093/mnras/stab839
Haardt, F., & Maraschi, L. 1991, ApJL, 380, L51, doi: 10.1086/186171
Harris, C. R., Millman, K. J., van der Walt, S. J., et al. 2020, Nature, 585, 357, doi: 10.1038/s41586-020-2649-2
Hernán-Caballero, A., Willmer, C. N. A., Varela, J., et al. 2023, arXiv e-prints, arXiv:2301.09623, doi: 10.48550/arXiv.2301.09623
HI4PI Collaboration, Ben Bekhti, N., Flöer, L., et al. 2016, A&A, 594, A116, doi: 10.1051/0004-6361/201629178
Kalberla, P. M. W., Burton, W. B., Hartmann, D., et al. 2005, A&A, 440, 775, doi: 10.1051/0004-6361:20041864
Kammoun, E., Lohfink, A. M., Masterson, M., et al. 2024, Frontiers in Astronomy and Space Sciences, 10, 1308056, doi: 10.3389/fspas.2023.1308056
Kormendy, J., & Ho, L. C. 2013, ARA&A, 51, 511, doi: 10.1146/annurev-astro-082708-101811
Kuraszkiewicz, J., Wilkes, B. J., Atanas, A., et al. 2021, ApJ, 913, 134, doi: 10.3847/1538-4357/abf3c0
LaMassa, S. M., Heckman, T. M., Ptak, A., et al. 2009, ApJ, 705, 568, doi: 10.1088/0004-637X/705/1/568

Lansbury, G. B., Stern, D., Aird, J., et al. 2017, ApJ, 836, 99, doi: 10.3847/1538-4357/836/1/99
Lanzuisi, G., Civano, F., Marchesi, S., et al. 2018, MNRAS, 480, 2578, doi: 10.1093/mnras/sty2025
Liedahl, D. A., Osterheld, A. L., & Goldstein, W. H. 1995, ApJL, 438, L115, doi: 10.1086/187729
Marchesi, S., Zhao, X., Torres-Albà, N., et al. 2022, ApJ, 935, 114, doi: 10.3847/1538-4357/ac80be
Markowitz, A. G., Krumpe, M., & Nikutta, R. 2014, MNRAS, 439, 1403, doi: 10.1093/mnras/stt2492
Martocchia, A., & Matt, G. 1996, MNRAS, 282, L53, doi: 10.1093/mnras/282.4.L53
Masini, A., Civano, F., Comastri, A., et al. 2018, ApJS, 235, 17, doi: 10.3847/1538-4365/aaa83d
Matt, G., & Iwasawa, K. 2019, MNRAS, 482, 151, doi: 10.1093/mnras/sty2697
Mewe, R., Gronenschild, E. H. B. M., & van den Oord, G. H. J. 1985, A&AS, 62, 197
Mewe, R., Lemen, J. R., & van den Oord, G. H. J. 1986, A&AS, 65, 511
Mineo, S., Gilfanov, M., & Sunyaev, R. 2012, MNRAS, 426, 1870, doi: 10.1111/j.1365-2966.2012.21831.x
Mullaney, J. R., Del-Moro, A., Aird, J., et al. 2015, ApJ, 808, 184, doi: 10.1088/0004-637X/808/2/184
Nandra, K., & Pounds, K. A. 1994, MNRAS, 268, 405, doi: 10.1093/mnras/268.2.405
Nenkova, M., Sirocky, M. M., Ivezić, Ž., & Elitzur, M. 2008a, ApJ, 685, 147, doi: 10.1086/590482
Nenkova, M., Sirocky, M. M., Nikutta, R., Ivezić, Ž., & Elitzur, M. 2008b, ApJ, 685, 160, doi: 10.1086/590483
O'Brien, R., Jansen, R. A., Grogin, N. A., et al. 2024, ApJS, 272, 19, doi: 10.3847/1538-4365/ad3948
Peca, A., Cappelluti, N., Urry, C. M., et al. 2023, ApJ, 943, 162, doi: 10.3847/1538-4357/acac28
Pfeifle, R. W., Boorman, P. G., Weaver, K. A., et al. 2024, Frontiers in Astronomy and Space Sciences, 11, 1304652, doi: 10.3389/fspas.2024.1304652
Piotrowska, J. M., García, J. A., Walton, D. J., et al. 2024, Frontiers in Astronomy and Space Sciences, 11, 1324796, doi: 10.3389/fspas.2024.1324796
Planck Collaboration, Aghanim, N., Akrami, Y., et al. 2020, A&A, 641, A6, doi: 10.1051/0004-6361/201833910
Price-Whelan, A. M., Sipőcz, B. M., Günther, H. M., et al. 2018, AJ, 156, 123, doi: 10.3847/1538-3881/aabc4f
Ricci, C., Ueda, Y., Koss, M. J., et al. 2015, ApJL, 815, L13, doi: 10.1088/2041-8205/815/1/L13
Ricci, C., Trakhtenbrot, B., Koss, M. J., et al. 2017, ApJS, 233, 17, doi: 10.3847/1538-4365/aa96ad
Risaliti, G., Maiolino, R., & Salvati, M. 1999, ApJ, 522, 157, doi: 10.1086/307623
Rossland, S., Wik, D. R., Grefenstette, B., et al. 2023, AJ, 166, 20, doi: 10.3847/1538-3881/acd0ae
Schlafly, E. F., Meisner, A. M., & Green, G. M. 2019, ApJS, 240, 30, doi: 10.3847/1538-4365/aafbea
Silver, R., Torres-Albà, N., Zhao, X., et al. 2022, ApJ, 940, 148, doi: 10.3847/1538-4357/ac9bf8
Silver, R., Civano, F., Zhao, X., et al. 2025
Soltan, A. 1982, MNRAS, 200, 115, doi: 10.1093/mnras/200.1.115
Torres-Albà, N., Marchesi, S., Zhao, X., et al. 2023, A&A, 678, A154, doi: 10.1051/0004-6361/202345947
—. 2021, ApJ, 922, 252, doi: 10.3847/1538-4357/ac1c73
Torres-Albà, N., Hu, Z., Cox, I., et al. 2025, ApJ, 981, 91, doi: 10.3847/1538-4357/adaf18
Treister, E., Urry, C. M., & Virani, S. 2009, ApJ, 696, 110, doi: 10.1088/0004-637X/696/1/110
Turner, T. J., George, I. M., Nandra, K., & Mushotzky, R. F. 1997, ApJS, 113, 23, doi: 10.1086/313053
Ueda, Y., Akiyama, M., Hasinger, G., Miyaji, T., & Watson, M. G. 2014, ApJ, 786, 104, doi: 10.1088/0004-637X/786/2/104
Urry, C. M., & Padovani, P. 1995, PASP, 107, 803, doi: 10.1086/133630
Virtanen, P., Gommers, R., Oliphant, T. E., et al. 2020, Nature Methods, 17, 261, doi: 10.1038/s41592-019-0686-2
Wik, D. R., Hornstrup, A., Molendi, S., et al. 2014, ApJ, 792, 48, doi: 10.1088/0004-637X/792/1/48
Wilkes, B. J., Kuraszkiewicz, J., Haas, M., et al. 2013, ApJ, 773, 15, doi: 10.1088/0004-637X/773/1/15
Willmer, C. N. A., Ly, C., Kikuta, S., et al. 2023, ApJS, 269, 21, doi: 10.3847/1538-4365/acf57d
Windhorst, R. A., Cohen, S. H., Jansen, R. A., et al. 2023, AJ, 165, 13, doi: 10.3847/1538-3881/aca163
Yang, G., Boquien, M., Buat, V., et al. 2020, MNRAS, 491, 740, doi: 10.1093/mnras/stz3001
Yaqoob, T. 2012, MNRAS, 423, 3360, doi: 10.1111/j.1365-2966.2012.21129.x
Zappacosta, L., Comastri, A., Civano, F., et al. 2018, ApJ, 854, 33, doi: 10.3847/1538-4357/aaa550
Zhao, X., Civano, F., Fornasini, F. M., et al. 2021, MNRAS, 508, 5176, doi: 10.1093/mnras/stab2885
Zhao, X., Civano, F., Willmer, C. N. A., et al. 2024, ApJ, 965, 188, doi: 10.3847/1538-4357/ad2b61

Table 6. NuSTAR Spectral Extraction Region Sizes

	FPMA				FPMB					FPMA				FPMB			
	Cycle				Cycle					Cycle				Cycle			
ID	5	6	8	9	5	6	8	9	ID	5	6	8	9	5	6	8	9
1	20”	-	25”	15”	35”	-	15”	35”	31	15”	20”	40”	10”	15”	20”	30”	15”
2	20”	-	35”	50”	30”	-	40”	30”	32	15”	35”	45”	40”	20”	20”	45”	35”
3	35”	15”	15”	20”	20”	20”	15”	45”	33	20”	20”	15”	15”	30”	20”	15”	20”
4	55”	25”	30”	45”	10”	50”	55”	40”	34	20”	15”	15”	15”	25”	15”	35”	10”
5	20”	30”	50”	25”	20”	50”	35”	40”	35	15”	10”	15”	30”	15”	10”	10”	30”
6	25”	25”	35”	30”	25”	25”	30”	25”	36	40”	40”	45”	35”	25”	25”	40”	20”
7	25”	40”	30”	40”	20”	30”	25”	25”	37	20”	15”	35”	40”	20”	25”	35”	40”
8	20”	30”	20”	10”	20”	10”	20”	30”	38	60”	40”	40”	-	40”	45”	40”	-
9	10”	20”	40”	10”	25”	25”	15”	10”	39	20”	20”	30”	35”	30”	10”	30”	30”
10	15”	20”	20”	20”	20”	35”	30”	55”	40	15”	25”	10”	20”	10”	20”	25”	25”
11	20”	20”	25”	25”	35”	20”	25”	35”	41	40”	25”	25”	30”	35”	20”	30”	25”
12	25”	25”	15”	45”	35”	20”	25”	25”	42	20”	15”	35”	30”	40”	10”	20”	55”
13	25”	25”	15”	20”	15”	20”	20”	30”	43	25”	20”	45”	55”	15”	25”	35”	20”
14	25”	30”	40”	40”	15”	25”	40”	50”	44	20”	15”	40”	45”	10”	30”	15”	15”
15	20”	30”	20”	10”	20”	20”	15”	10”	45	20”	20”	20”	15”	20”	20”	25”	25”
16	15”	25”	40”	35”	55”	55”	30”	65”	46	10”	20”	20”	20”	20”	20”	20”	15”
17	30”	15”	15”	20”	20”	40”	10”	20”	47	20”	25”	35”	15”	20”	30”	45”	20”
18	10”	20”	25”	20”	40”	15”	50”	55”	48	35”	20”	30”	35”	30”	25”	40”	25”
19	20”	25”	50”	25”	40”	45”	50”	20”	49	15”	15”	25”	45”	15”	20”	10”	20”
20	25”	-	35”	45”	10”	-	10”	40”	50	20”	20”	10”	35”	20”	30”	15”	10”
21	20”	20”	25”	30”	20”	20”	35”	20”	51	20”	20”	20”	40”	20”	20”	20”	20”
22	20”	20”	10”	25”	20”	20”	10”	25”	52	20”	30”	10”	20”	20”	15”	10”	15”
23	40”	10”	10”	10”	10”	40”	40”	20”	53	20”	20”	40”	30”	20”	20”	25”	25”
24	25”	35”	25”	30”	40”	20”	15”	15”	54	35”	20”	25”	40”	45”	30”	45”	65”
25	-	20”	10”	75”	-	25”	10”	40”	55	30”	35”	25”	35”	25”	40”	30”	40”
26	15”	25”	15”	25”	15”	25”	20”	25”	56	20”	15”	25”	10”	25”	25”	25”	30”
27	15”	20”	55”	65”	30”	20”	55”	25”	57	50”	15”	20”	30”	35”	25”	45”	45”
28	20”	25”	20”	25”	20”	25”	35”	25”	58	45”	40”	25”	50”	35”	30”	25”	30”
29	35”	40”	50”	45”	35”	35”	40”	45”	59	20”	20”	20”	50”	20”	10”	30”	25”
30	30”	20”	20”	25”	25”	10”	35”	30”	60	20”	20”	30”	40”	20”	20”	15”	15”

APPENDIX

A. NUSTAR SOURCE EXTRACTION REGIONS

As the first step of spectral extraction, each source in the Z24 catalog is assigned a circular region centered around its NuSTAR position. The size of the region (radius r in arc-seconds) is chosen to maximize the signal-to-noise ratio using the equation presented in Zappacosta et al. (2018):

$$\mathrm{SNR}(<r) = \frac{N(<r)}{\sqrt{N(<r) + 2B(<r)}} \tag{A1}$$

Where $N(<r)$ is the total (not background-subtracted) number of counts extracted from a region with radius r centered around the source, and $B(<r)$ is the number of counts extracted from the background maps produced by NUSKYBGD. The SNR-maximized region sizes were determined separately for both FPMA and FPMB in each cycle. When necessary, region sizes were manually adjusted to prevent overlap and avoid contamination from bright sources. Table 6 shows the resulting region sizes for all sources and observations. A dash indicates that the source fell outside of the FOV for every observation within that cycle. All sources have

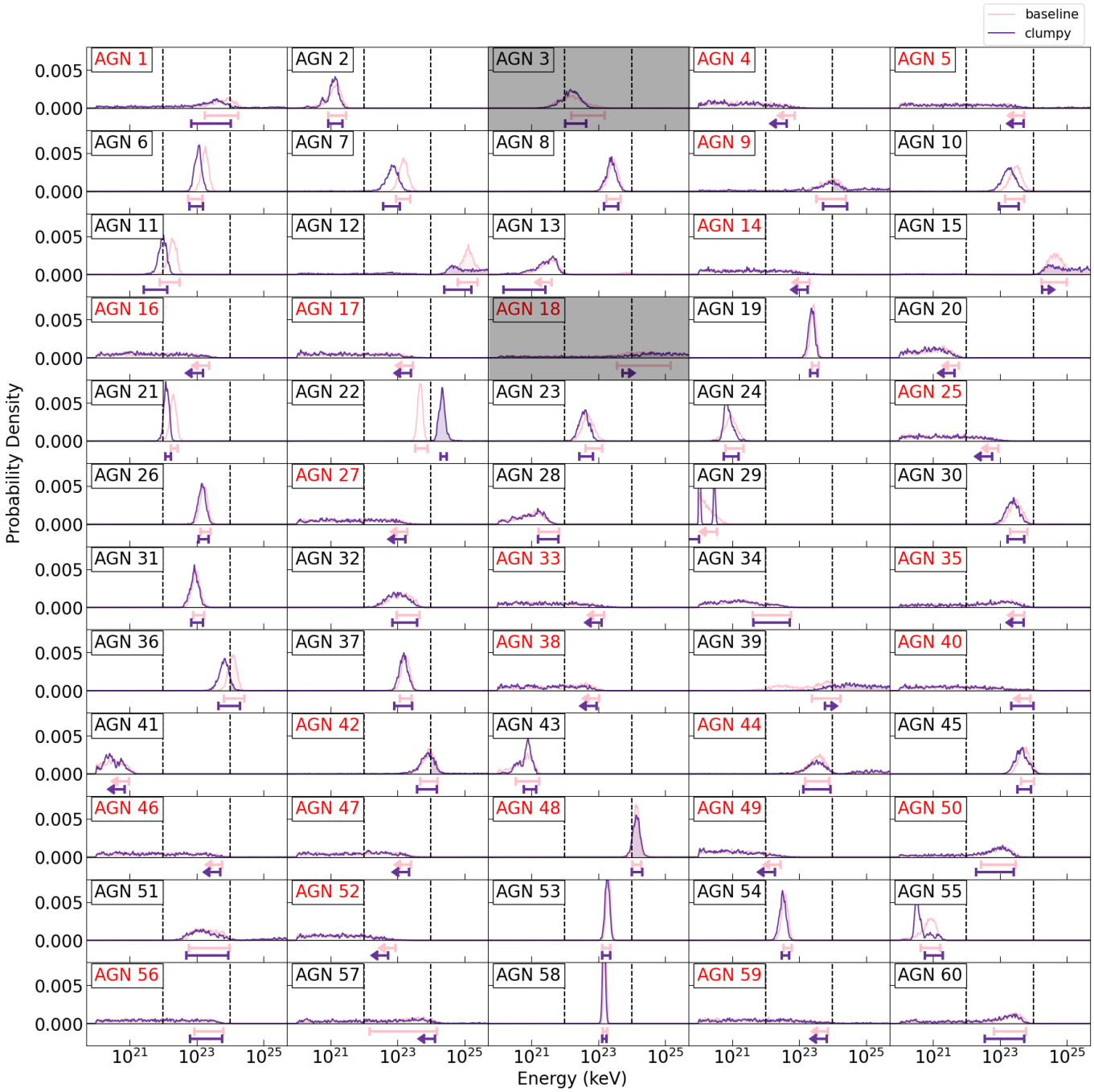

Figure 12. The posterior distributions for $N_{\rm H}$ found by BXA using both baseline (pink) and clumpy (purple) models. The vertical dashed line in each panel indicates the CT threshold, and CT portions of each posterior are shaded. The errorbar under the posterior distributions indicate the frequentest results for that source found using the standard XSPEC routines. Red labels indicate that XMM-Newton spectra did not exist for that source. Objects excluded from the analysis are shaded in gray.

extraction region sizes between 10″ and 75″, and 95% of source regions have radii < 50″.

We verified the spectral extraction process by comparing spectral counts to the photometric counts reported by Z24. Because Z24 uses $r = 20''$ for all sources in their analysis, spectral counts for this test were also extracted from 20″ regions in every Cycle 5+6 observation. Comparing net (background-subtracted) spectral counts to the net photometric counts yields a median difference (spec-phot) of $0.0^{+4.0}_{-2.0}$ and a median normalized difference (spec-phot/spec+phot) of $0.00^{+0.03}_{-0.02}$. Therefore, we conclude that the net source counts in the spectra are consistent with the photometry.

B. FIT DETAILS

The normalized PDFs derived from the BXA posteriors (see Section 3.3) are shown in Figures 12 (individual PDFs) and 13 (summed PDFs from the entire sample). Table 7 shows the best-fit parameters and 3σ errors for each source. Frozen parameters are given without error-bars. Figure 14 shows the best-fit model (using XSPEC's EEMODEL) and corresponding delta-chi residuals for each source.

B.1. *Notes on Individual Sources*

For both AGNs 36 and 54, there is an excess of emission in the FPMB spectrum at < 5 keV that is not fit by the model. This excess does not appear in FPMA, and ignoring the excess bins has no significant effects on the fit. Both objects have XMM data that are consistent with the best fit model, and $N_{\rm H}$ is well constrained (Figure 12), so we conclude that the excess is not cause for concern.

When fitting AGN 60, we find that the XMM-Newton and NuSTAR data are inconsistent. The best-fit model matches the XMM-Newton data well, but it underestimates the NuSTAR spectra. Similarly, when we fit exclusively to NuSTAR, the XMM-Newton spectra are overestimated by a factor of ~ 3. We conclude that the match between NuSTAR and XMM-Newton may be erroneous, so we only fit to the NuSTAR data.

Similarly, attempting to fit AGN 57 to both XMM-Newton and NuSTAR yields unphysical results. The best-fit models are CT with a lower limit on $N_{\rm H}$ (clumpy model) and an unconstrained scattered component (both models). When XMM-Newton is excluded, a scattered component is not required and the constraints on $N_{\rm H}$ are reasonable, with upper error bars in the CT regime. We conclude that the fit is more trustworthy when XMM-Newton is excluded.

B.1.1. *CT Candidates*

Similar to AGNs 36 and 54, several of our CT candidates (AGNs 9, 18, and 48) had excess counts in the softest bins of one—but not both—of the NuSTAR instruments, and the excess counts do not contribute to the best-fit model. We discuss those objects in more detail here.

AGN 9: Visually, this object does not appear to be CT due to high counts at 3 keV—the softest part of the NuSTAR spectrum— for FPMA. However, the best fit model strongly prefers to be CT. The CT classification appears to be driven by low counts (in both NuSTAR instruments) at ∼5 keV. Since this object was not matched to any XMM sources, we conclude that more data is needed to accurately fit it, but we chose to include it in the analysis.

AGN 18: Similar to AGN 9, this object is faint and dominated by the background. It does not visually appear to be CT, but the best-fit model strongly prefers high values of $N_{\rm H}$. However, $N_{\rm H}$ is poorly constrained for both the baseline and clumpy models (see Figure 12) and fits for the galactic component are not consistent between the two (Figure 14). For these reasons, we have decided that this fit is untrustworthy, and we do not include it in the analysis.

AGN 48: The excess emission for AGN 48 occurs in FPMA at < 4.0 keV. This emission does not affect the best fit, which is well constrained to be CT. Further, when we ignore the bins with the excess counts, the spectral cutoff at < 9 keV is visually clear, is consistent between FPMA and FPMB, and fits well to the model. Therefore we determine that this fit is trustworthy.

Table 7. Best-Fit Model Parameters

		baseline						clumpy					
ID[a]	pass (y/n)[b]	Γ	nH (10^{22} cm^{-2})	$-\log(F)^c$	n^d	f^e	C/DOF	Γ	nH (10^{22} cm^{-2})	κ^f	n^d	f^e	C/DOF
1	n	1.80	80.7^{+93}_{-63}	$13.3^{+0.3}_{-0.4}$	-	-	144.2/155	1.80	39.9^{+64}_{-33}	$2.3^{+3.9}_{-1.4}$	-	-	144.7/155
2	n	$1.99^{+0.13}_{-0.12}$	$0.2^{+0.1}_{-0.1}$	$13.3^{+0.1}_{-0.1}$	$1.1^{+0.5}_{-0.5}$	-	751.8/740	$1.98^{+0.13}_{-0.05}$	$0.2^{+0.1}_{-0.1}$	$8.3^{+0.7}_{-5}$	$8.3^{+-5.8}_{--1.4}$	-	743.8/740
3	n	1.80	$4.4^{+11}_{-2.9}$	$13.8^{+0.2}_{-0.2}$	-	≥ 2.6	357.4/413	1.80	$2.1^{+2.2}_{-1.1}$	$0.6^{+0.2}_{-0.3}$	$0.6^{+-0.5}_{--0.3}$	-	355.1/413
4	n	1.80	≤ 7.3	$13.5^{+0.1}_{-0.1}$	-	-	622.5/646	1.80	≤ 4.4	$1.8^{+1.7}_{-0.4}$	-	-	621.4/646

Table 7 *continued*

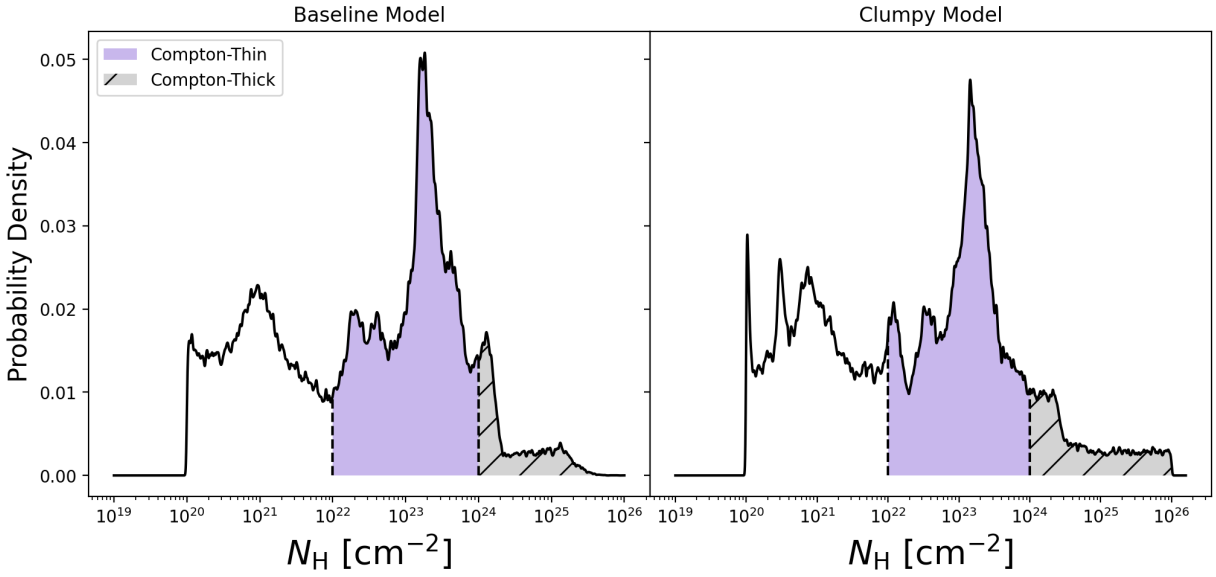

Figure 13. The added probability density functions (PDFs) of the sample for the baseline (left) and clumpy (right) models, giving the observed $N_{\rm H}$ distribution. The sum under the curve in the C-Thin (purple; solid) and CT (gray; hatched) regimes gives the effective C-Thin and CT sample size.

Table 7 *(continued)*

5	n	1.80	≤ 53.4	$13.8^{+0.4}_{-0.3}$	-	-	472.7/518	1.80	≤ 50.8	$0.5^{+0.2}_{-0.2}$	-	-	472.4/518
6	y	$1.48^{+0.28}_{-0.26}$	$9.7^{+5.5}_{-4.1}$	$13.4^{+0.1}_{-0.1}$	$0.1^{+0.1}_{-0.1}$	-	598.4/600	$1.6^{+0.32}_{-0.22}$	$9.2^{+6.5}_{-3.1}$	$2.5^{+3.1}_{-1.1}$	$2.5^{+-2.2}_{--1.2}$	-	599.9/600
7	n	1.80	$14.4^{+9.4}_{-5.4}$	$13.3^{+0.1}_{-0.1}$	$0.2^{+0.1}_{-0.1}$	-	477.0/559	1.80	$7^{+5}_{-3.2}$	$1.5^{+0.4}_{-0.5}$	$1.5^{+-1.2}_{--0.8}$	-	477.3/559
8	n	1.80	28.9^{+17}_{-11}	$13.5^{+0.1}_{-0.2}$	-	-	235.0/239	1.80	25.5^{+15}_{-10}	$3.4^{+1.4}_{-1.2}$	-	-	235.7/239
9	n	1.80	$109^{+1.4e+02}_{-75}$	$13^{+0.3}_{-0.3}$	-	-	130.4/130	1.80	$93.6^{+1.8e+02}_{-42}$	$10.1^{+27}_{-6.2}$	-	-	132.3/133
10	n	1.80	27.6^{+26}_{-14}	$13.8^{+0.2}_{-0.2}$	-	≥ 3.9	476.8/526	1.80	19.8^{+17}_{-10}	$1.5^{+0.7}_{-0.6}$	$1.5^{+-1.3}_{--0.7}$	-	479.5/526
11	n	$1.72^{+0.49}_{-0.43}$	$1.8^{+1.3}_{-1}$	$13.9^{+0.2}_{-0.2}$	-	-	487.5/491	$1.5^{+0.31}_{-0.2}$	$0.8^{+0.5}_{-0.5}$	$0.5^{+0.2}_{-0.3}$	-	-	472.6/491
12	n	1.80	$1.2e+03^{+1.2e+03}_{-5.8e+02}$	$13.7^{+0.2}_{-0.1}$	-	≥ 6.0	568.7/598	1.80	$439^{+1.2e+03}_{-1.9e+02}$	40.4^{+13}_{-12}	-	≥ 4.8	584.6/598
13	n	1.80	≤ 0.4	$14^{+0.1}_{-0.1}$	-	≥ 0.0	591.2/634	1.80	$0.1^{+0.2}_{-0.1}$	$0.1^{+0.1}_{-0.1}$	-	-	589.5/635
14	n	1.80	≤ 20.3	$13.7^{+0.2}_{-0.2}$	-	-	469.3/524	1.80	≤ 18.0	$0.7^{+0.5}_{-0.2}$	-	-	468.9/524
15	n	1.80	$409^{+5.7e+02}_{-2.4e+02}$	$13.5^{+0.2}_{-0.2}$	-	≥ 3.9	250.4/276	1.80	≥ 179.2	$19.7^{+9.9}_{-6.3}$	-	≥ 5.9	257.3/276
16	n	1.80	≤ 23.4	$13.7^{+0.2}_{-0.2}$	-	-	395.2/430	1.80	≤ 15.3	$0.4^{+2.1}_{-0.1}$	-	-	394.4/430
17	y	1.80	≤ 28.3	$13.5^{+0.2}_{-0.2}$	-	-	307.1/324	1.80	≤ 25.4	$1.1^{+1}_{-0.4}$	-	-	306.8/324
18	n	1.80	$123^{+1.3e+03}_{-87}$	$13.1^{+1.1}_{-0.5}$	85.5^{+63}_{-57}	-	357.1/353	1.80	≥ 52.4	15.5^{+10}_{-14}	-	-	361.2/354
19	n	1.80	$31.1^{+8.3}_{-6.6}$	$13.5^{+0.1}_{-0.1}$	$0.3^{+0.2}_{-0.1}$	-	884.3/914	1.80	$26.8^{+8.4}_{-5.8}$	$6.1^{+1.2}_{-0.9}$	$6.1^{+-5.5}_{--4.8}$	-	882.4/914
20	n	$1.7^{+0.41}_{-0.28}$	≤ 0.6	$14^{+0.1}_{-0.2}$	-	-	448.6/458	$1.69^{+0.3}_{-0.21}$	≤ 0.4	$0.7^{+1.3}_{-0.1}$	-	-	446.5/458
21	y	1.80	$2.2^{+0.5}_{-0.5}$	13.5^{+0}_{-0}	-	≥ 6.8	674.6/692	1.80	$1.5^{+0.3}_{-0.3}$	$2.2^{+0.5}_{-0.4}$	$2.2^{+-2}_{--1.6}$	-	677.7/692
22	y	$1.95^{+0.49}_{-0.4}$	52.7^{+26}_{-18}	$13.4^{+0.2}_{-0.1}$	-	-	461.8/456	1.80	224^{+70}_{-26}	$56.5^{+14}_{-8.7}$	-	-	491.1/457
23	n	1.80	$7.3^{+5.8}_{-3.1}$	$13.7^{+0.1}_{-0.1}$	-	≥ 1.6	427.9/488	1.80	$4.4^{+2.6}_{-1.6}$	$1.2^{+0.5}_{-0.3}$	$1.2^{+-1.1}_{--0.9}$	-	429.2/488
24	y	$1.72^{+0.09}_{-0.09}$	$0.1^{+0.1}_{-0.1}$	13.3^{+0}_{-0}	$0.3^{+0.3}_{-0.2}$	-	714.5/723	$1.73^{+0.07}_{-0.08}$	$0.1^{+0.1}_{-0}$	$2.7^{+2.4}_{-0.9}$	$2.7^{+-2}_{--1.4}$	-	714.2/723
25	y	1.80	≤ 9.0	$13.4^{+0.1}_{-0.1}$	-	-	394.5/379	1.80	≤ 5.8	$0.8^{+2.1}_{-0.2}$	-	-	394.0/379
26	n	1.80	$18.5^{+7.3}_{-5.2}$	$13.7^{+0.1}_{-0.1}$	-	-	461.7/456	1.80	$16.6^{+6.4}_{-5}$	$4.6^{+1.2}_{-1}$	-	-	459.4/456
27	n	1.80	≤ 19.8	$13.6^{+0.2}_{-0.2}$	-	-	659.2/740	1.80	≤ 17.1	$0.6^{+0.5}_{-0.2}$	-	-	658.6/740
28	y	1.80	$0.4^{+0.3}_{-0.2}$	$13.8^{+0.1}_{-0.1}$	$0.3^{+0.1}_{-0.1}$	-	850.0/826	1.80	$0.3^{+0.3}_{-0.2}$	$1.1^{+0.6}_{-0.2}$	$1.1^{+-0.4}_{--0.4}$	-	845.8/826
29	y	$1.62^{+0.02}_{-0.02}$	≤ 0.0	12.7^{+0}_{-0}	$1.5^{+1}_{-0.7}$	-	2060.5/2050	$1.69^{+0.02}_{-0.01}$	≤ 0.0	$22^{+2.3}_{-0.8}$	-	≥ 0.0	2047.8/2050
30	n	1.80	38.4^{+27}_{-18}	$13.7^{+0.1}_{-0.2}$	-	-	515.3/520	1.80	32^{+22}_{-15}	$4.6^{+2.2}_{-1.6}$	-	-	514.4/520
31	y	1.80	$11.4^{+5.9}_{-3.5}$	$13.4^{+0.1}_{-0.1}$	-	-	485.8/441	1.80	$10.5^{+4.9}_{-3.6}$	$2.5^{+0.5}_{-0.4}$	-	-	483.9/441
32	n	1.80	26.6^{+20}_{-17}	$14^{+0.1}_{-0.2}$	-	-	658.8/760	1.80	22.8^{+15}_{-16}	$2.6^{+1.1}_{-1.1}$	-	-	661.8/765
33	n	1.80	≤ 15.0	$13.7^{+0.2}_{-0.2}$	-	-	214.5/203	1.80	≤ 12.8	$1.1^{+0.8}_{-0.6}$	-	-	214.3/203
34	n	1.80	$2.2^{+3.5}_{-1.8}$	$14.2^{+0.2}_{-0.3}$	0.1^{+0}_{-0}	-	401.3/454	1.80	$2.6^{+2.8}_{-2.1}$	$0.5^{+0.2}_{-0.3}$	$0.5^{+-0.3}_{--0.1}$	-	400.3/454
35	n	1.80	≤ 53.5	$13.5^{+0.3}_{-0.3}$	-	-	259.6/247	1.80	≤ 50.7	$1.1^{+1.5}_{-0.6}$	-	-	259.6/247
36	n	$2.06^{+1.1}_{-0.82}$	$152^{+1.2e+02}_{-87}$	$13.5^{+0.3}_{-0.3}$	-	≥ 0.1	738.4/733	$2.17^{+0.81}_{-0.54}$	94.3^{+1e+02}_{-50}	≤ 271.3	-	≥ 0.1	745.5/735

Table 7 *continued*

Table 7 *(continued)*

37	n	1.80	$17.6^{+8.8}_{-5.7}$	$13.6^{+0.1}_{-0.1}$	-	-	537.2/575	$1.8^{+0.58}_{-0.42}$	$15.4^{+13}_{-7.4}$	≤ 13.7	-	-	537.7/574
38	n	1.80	≤ 10.8	$12.7^{+0.1}_{-0.1}$	-	-	297.3/299	1.80	≤ 9.0	≤ 8.3	-	-	296.1/299
39	y	1.80	82.8^{+92}_{-58}	$13.3^{+0.2}_{-0.3}$	-	≥ 2.0	242.0/238	1.80	≥ 58.5	≤ 90.2	-	-	250.6/239
40	y	1.80	≤ 81.3	$13.3^{+0.6}_{-0.1}$	-	-	187.7/229	1.80	51.1^{+48}_{-29}	$2.9^{+2.7}_{-1.4}$	-	≥ 3.2	187.5/229
41	y	$1.56^{+0.19}_{-0.12}$	≤ 0.1	$13.9^{+0.1}_{-0.1}$	-	-	774.9/794	$1.58^{+0.09}_{-0.1}$	≤ 0.1	$0.9^{+0.7}_{-0.1}$	-	-	772.0/794
42	y	1.80	94.4^{+65}_{-46}	$13.1^{+0.2}_{-0.3}$	≤ 41.8	-	339.2/376	1.80	79.4^{+71}_{-41}	3.4^{+4}_{-2}	$3.4^{+52}_{--1.4}$	-	340.2/376
43	y	$2.08^{+0.11}_{-0.1}$	$0.1^{+0.1}_{-0.1}$	$13.7^{+0}_{-0.1}$	-	-	1197.5/1150	$2.08^{+0.08}_{-0.07}$	$0.1^{+0.1}_{-0}$	$5^{+2.9}_{-2}$	-	-	1186.3/1150
44	y	1.80	38.9^{+41}_{-24}	$13.5^{+0.2}_{-0.2}$	-	-	453.8/503	1.80	36.2^{+49}_{-23}	$1.5^{+1.8}_{-0.7}$	-	-	453.0/503
45	y	1.80	68.3^{+36}_{-26}	$13.4^{+0.1}_{-0.1}$	-	-	546.2/543	1.80	49.7^{+36}_{-16}	$7.1^{+1.8}_{-1.8}$	-	-	544.9/543
46	y	1.80	≤ 58.7	$13.7^{+0.2}_{-0.2}$	-	-	297.6/337	1.80	≤ 50.9	$1.5^{+1.3}_{-0.7}$	-	-	296.7/337
47	y	1.80	≤ 25.7	$13.7^{+0.2}_{-0.2}$	-	-	520.8/603	1.80	≤ 22.7	$0.5^{+0.7}_{-0.1}$	-	-	520.3/603
48	y	1.80	141^{+46}_{-36}	$12.4^{+0.1}_{-0.1}$	-	-	290.2/300	1.80	144^{+61}_{-46}	$24.2^{+14}_{-9.9}$	-	-	292.0/300
49	n	1.80	≤ 2.8	$13.4^{+0.1}_{-0.1}$	-	-	249.3/278	1.80	≤ 1.9	$3.2^{+0.9}_{-2.6}$	-	-	248.6/278
50	n	1.80	13.1^{+16}_{-10}	$13.5^{+0.2}_{-0.2}$	-	-	363.0/390	1.80	10.9^{+15}_{-9}	$1.2^{+0.7}_{-0.4}$	-	-	363.5/390
51	n	1.80	$15.6^{+80}_{-9.7}$	$13.4^{+0.3}_{-0.2}$	-	-	289.7/318	1.80	$12.3^{+75}_{-7.4}$	$2.5^{+3.3}_{-0.7}$	-	-	288.3/318
52	n	$1.92^{+0.97}_{-0.73}$	≤ 8.7	$13.7^{+0.3}_{-0.2}$	-	-	335.1/358	1.80	≤ 5.4	$0.6^{+1.2}_{-0.2}$	-	-	335.4/359
53	y	$1.46^{+0.2}_{-0.19}$	$17.2^{+5.4}_{-4.2}$	$13.4^{+0.1}_{-0.1}$	-	-	784.4/771	$1.6^{+0.2}_{-0.18}$	$17.2^{+5.6}_{-4.3}$	$3.2^{+2.6}_{-1.3}$	-	-	784.4/771
54	y	1.80	$4.5^{+1.3}_{-1.1}$	$13.8^{+0.1}_{-0.1}$	$0.1^{+0.1}_{-0}$	-	926.2/993	1.80	4^{+1}_{-1}	$1.7^{+0.3}_{-0.3}$	$1.7^{+-1.5}_{--1.3}$	-	924.9/993
55	y	$1.66^{+0.05}_{-0.05}$	$0.1^{+0.1}_{-0.1}$	13^{+0}_{-0}	$0.8^{+0.4}_{-0.4}$	-	1277.7/1318	$1.72^{+0.03}_{-0.04}$	$0.2^{+0}_{-0.1}$	$7.6^{+1.1}_{-3.7}$	$7.6^{+-5.4}_{--2.1}$	-	1265.7/1318
56	n	1.80	33.4^{+30}_{-25}	$13.4^{+0.2}_{-0.2}$	57.1^{+37}_{-37}	-	353.2/359	1.80	28.6^{+28}_{-22}	$1.4^{+1.1}_{-0.7}$	$1.4^{+1.2e+02}_{-76}$	-	353.6/359
57	y	1.80	54.3^{+98}_{-53}	$13.4^{+0.1}_{-0.2}$	-	-	456.0/552	1.80	≤ 132.8	$7.4^{+6.4}_{-4}$	-	-	455.5/552
58	y	$1.83^{+0.15}_{-0.14}$	$16.2^{+2.6}_{-2.3}$	$12.7^{+0.1}_{-0}$	-	-	1026.6/1095	$1.92^{+0.15}_{-0.15}$	$15.2^{+2.7}_{-2.3}$	$12.1^{+6}_{-3.7}$	-	-	1020.2/1095
59	n	1.80	≤ 74.0	$13.8^{+0.5}_{-0.2}$	-	-	360.7/346	1.80	≤ 68.4	≤ 1.1	-	-	360.4/346
60	n	1.80	30.5^{+30}_{-24}	$13.3^{+0.1}_{-0.2}$	-	-	290.9/312	1.80	26.1^{+27}_{-23}	$3.4^{+1.8}_{-1.3}$	-	-	290.7/312

Note—

[a] NuSTAR IDs from the catalog by Z24

[b] Whether this object passed the 8-24 keV signal-to-noise and maximum likelihood requirements to be included in the Section 4.2 analysis.

[c] $-\log(F_{2-10}/\mathrm{erg\,cm^{-2}\,s^{-1}})$: Flux from 2–10 keV.

[d] Normalization of the MEKAL model: $\frac{10^{-14}}{4\pi[D_A(1+z)]^2}\int n_e n_H dV$

[e] Factor of scattered power law emission (omni component of UXCLUMPY)

[f] Normalization of the POWERLAW model: 10^{-3} photons $\mathrm{keV^{-1}\ cm^{-2}s^{-1}}$ at 1 keV

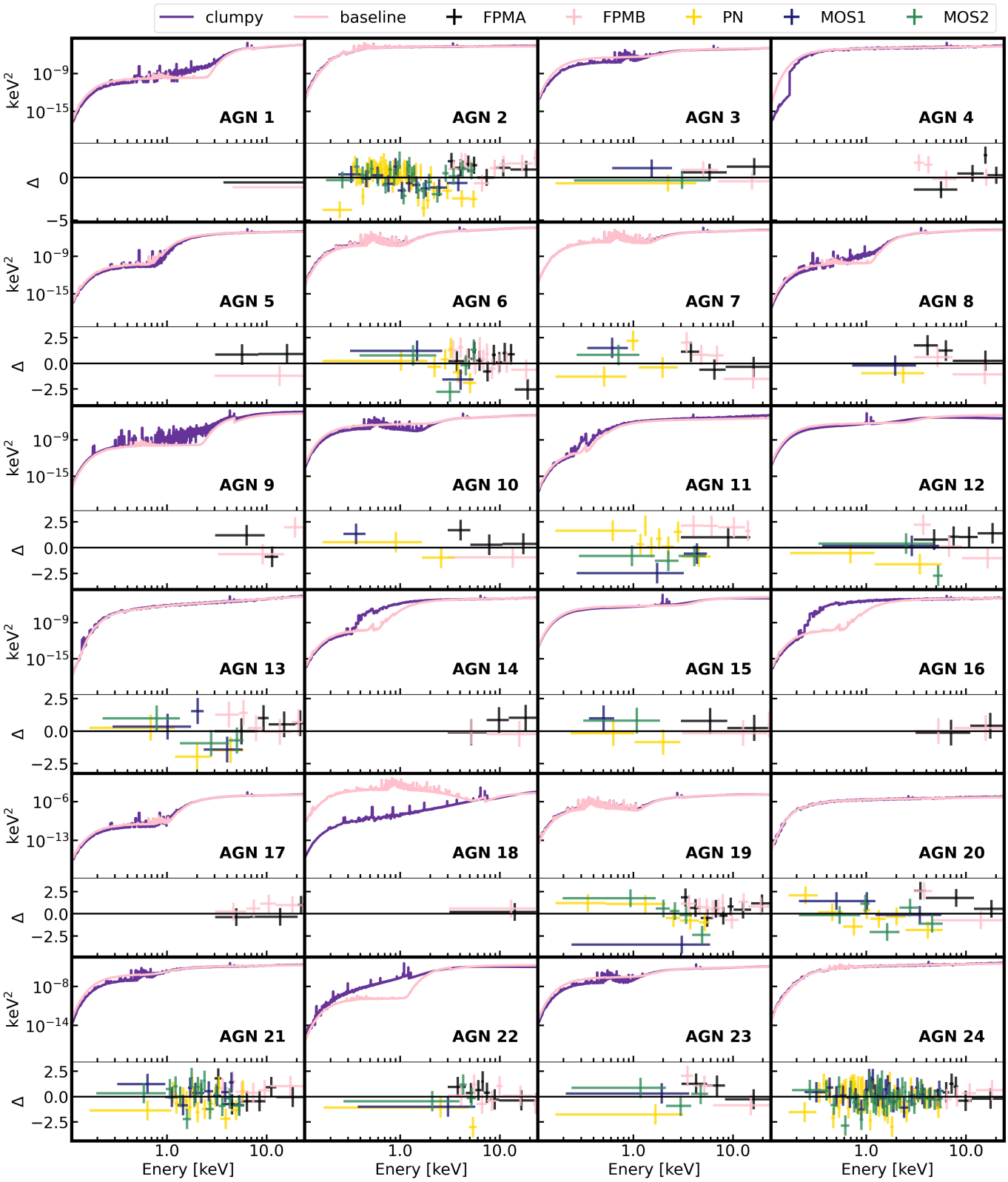
clumpy
baseline
FPMA
FPMB
PN
MOS1
MOS2
AGN 1
AGN 2
AGN 3
AGN 4
AGN 5
AGN 6
AGN 7
AGN 8
AGN 9
AGN 10
AGN 11
AGN 12
AGN 13
AGN 14
AGN 15
AGN 16
AGN 17
AGN 18
AGN 19
AGN 20
AGN 21
AGN 22
AGN 23
AGN 24
keV²
Δ
Enery [keV]

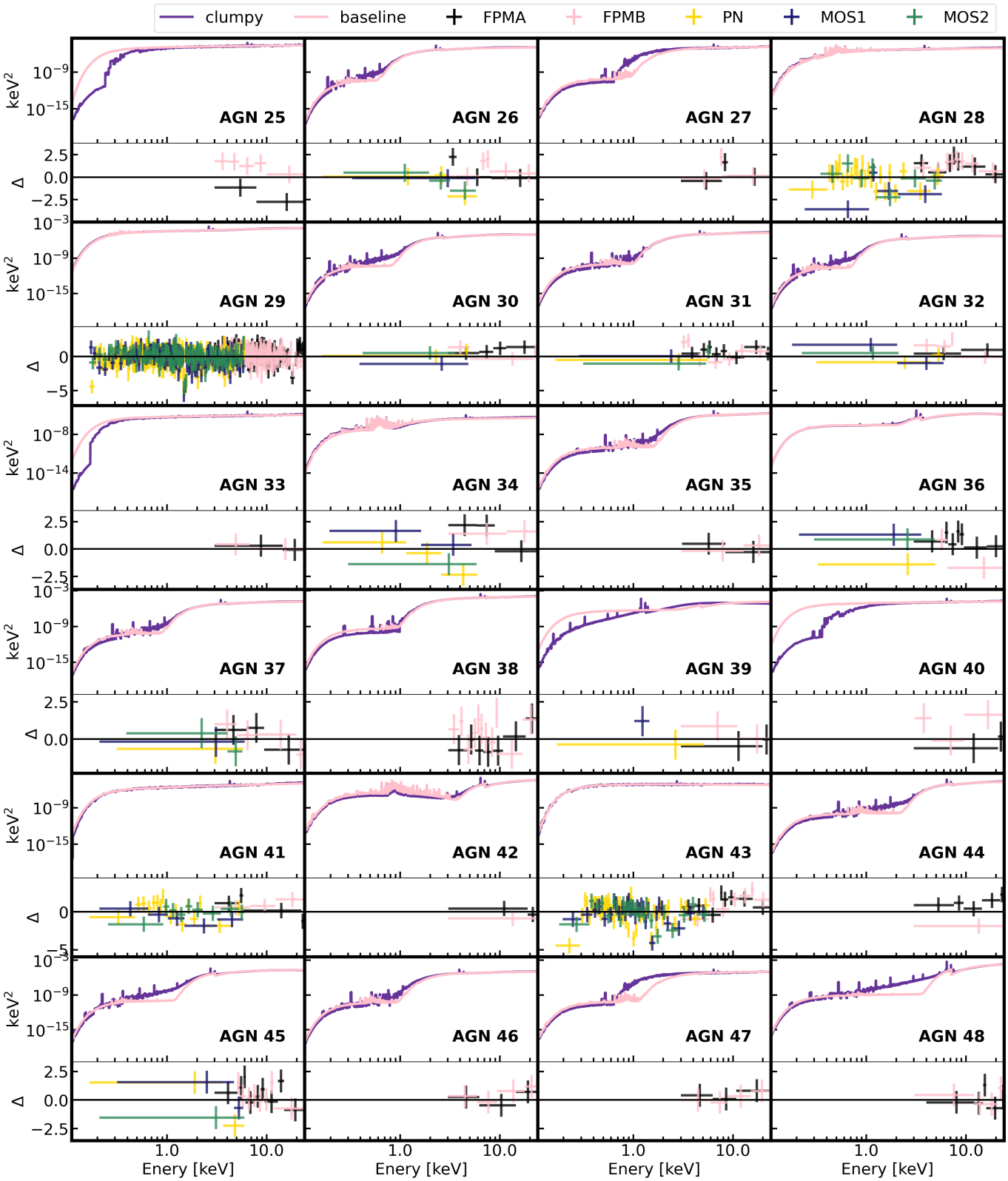
clumpy
baseline
FPMA
FPMB
PN
MOS1
MOS2
AGN 25
AGN 26
AGN 27
AGN 28
AGN 29
AGN 30
AGN 31
AGN 32
AGN 33
AGN 34
AGN 35
AGN 36
AGN 37
AGN 38
AGN 39
AGN 40
AGN 41
AGN 42
AGN 43
AGN 44
AGN 45
AGN 46
AGN 47
AGN 48
keV²
Δ
Enery [keV]

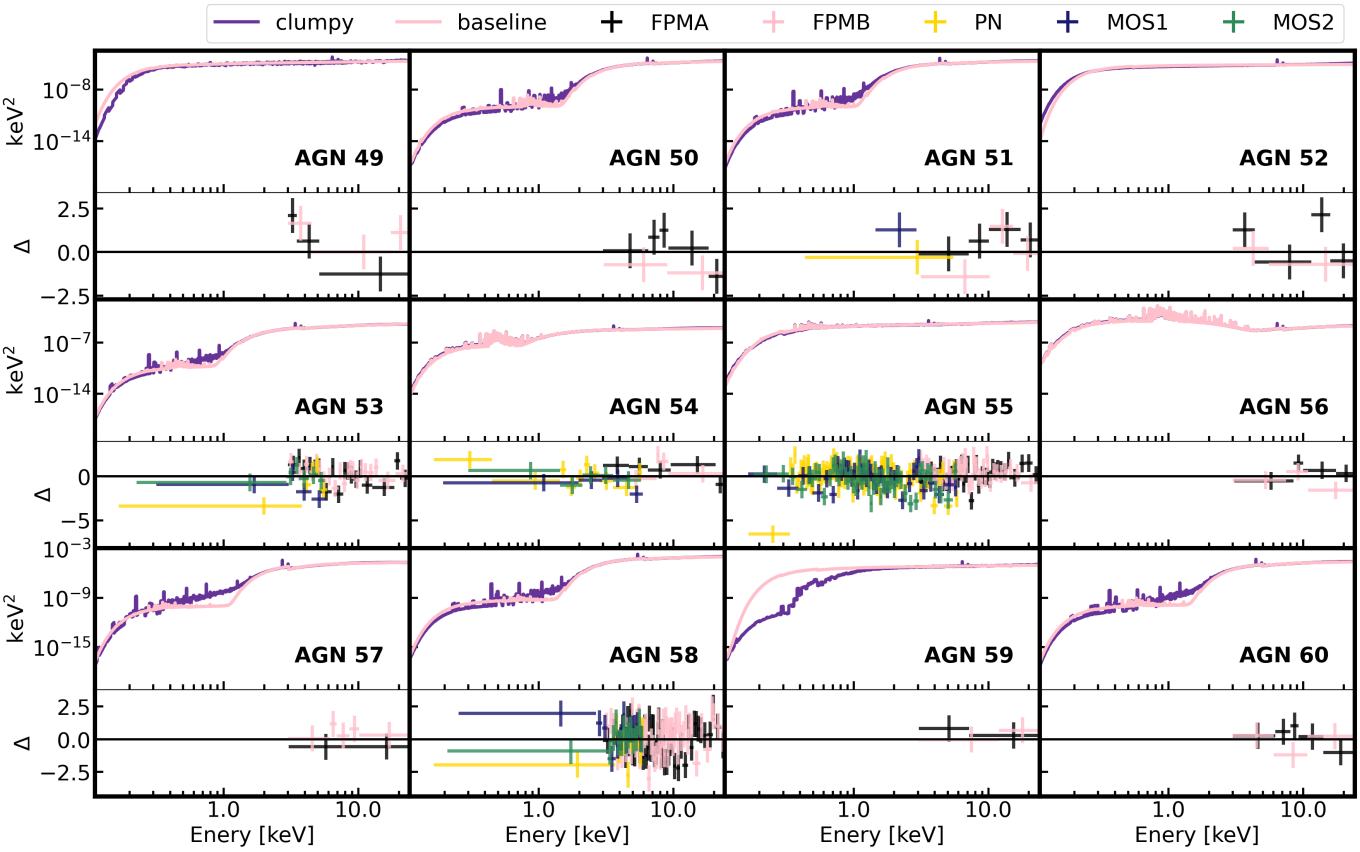

Figure 14. Best-fit clumpy (purple) and baseline (pink) EEMODEL for each source compared to the delta-chi error (Δ).